



The flow in the surf zone: a fully nonlinear Boussinesq-type of approach

Rosaria E. Musumeci^{a,*}, Ib A. Svendsen^{b,✱}, Jayaram Veeramony^c

^a*Department Civil and Environmental Engineering, University of Catania, Viale A. Doria 6, 95125, Catania, Italy*

^b*Center for Applied Coastal Research, University of Delaware, USA*

^c*Engineering Research Center, Mississippi State University, USA*

Received 1 April 2004; received in revised form 28 January 2005; accepted 10 February 2005

Available online 25 April 2005

Abstract

The dynamics of the wave propagation within the surf zone is represented through a weakly dispersive fully nonlinear Boussinesq-type of model. The flow is assumed rotational and the governing equations are derived with no assumptions on the order of magnitude of the nonlinear effects. In the modeling, the velocity field is influenced by the effects of vorticity due to breaking, and the vorticity transport equation is solved analytically. The amount of vorticity introduced by the breaking process is determined through an analogy with the hydraulic jump and the adoption of the concept of the surface roller.

A numerical accurate description of the effects of the surface roller is obtained by adopting an original self-adaptive-time-varying grid, developed on purpose. Such an approach makes it possible to get a better resolution in the region with rapid variations where the vorticity is generated, without heavily affecting the efficiency of the numerical model. Comparisons with a weakly nonlinear version of the model show that the proposed model considerably improves the estimate of the dynamics of wave propagations both in the shoaling and in the surf zone.

Comparisons with laboratory measurements, both for regular and irregular waves, demonstrate that the proposed model has fairly good prediction capabilities. In particular, in contrast to other models, it provides quite good estimates of both the velocity and the undertow profiles. Moreover, typical features of random wave breaking (such as varying breaking line, different wave height decay, effects of groupiness) can be reproduced by the proposed model, as shown through comparisons with group wave laboratory data.

© 2005 Elsevier B.V. All rights reserved.

Keywords: Surf zone hydrodynamics; Wave breaking; Fully nonlinear Boussinesq model; Vorticity; Wave groups

1. Introduction

Surf zone hydrodynamics, i.e. the hydrodynamics which takes place within the region extended from the breaking line up to the swash zone, not only is

* Corresponding author. Tel.: +39 095 7382727; fax: +39 095 7382748.

E-mail address: rmusume@dica.unict.it (R.E. Musumeci).

✱ Deceased.

interesting from the scientific point of view, but also from a practical one, since it strongly affects coastal processes such as sediment transport and littoral evolution.

Such phenomena are mainly influenced by wave breaking, which represents the main mechanism of dissipation of the energy associated with the organized wave motion. Furthermore, since waves approaching the shore undergo transformation processes before breaking, such a refraction and shoaling, the flow features within the surf zone as well as the extent of the surf zone itself are strongly affected by the conditions with which waves reach the breaking point.

Therefore an accurate description of surf zone hydrodynamics cannot be reproduced without appropriately looking also at the wave propagation phenomena within the shoaling region.

Over the last decades, starting for example from the work of Peregrine (1966), the Boussinesq equations have been widely developed to describe also surf zone hydrodynamics.

From a computational point of view such depth integrated models are more efficient compared with the more complex Navier–Stokes equations, and more accurate than the simpler nonlinear shallow water equations, since they provide more physically based results.

Due to these advantages, the scientific community has put many efforts into overcoming some of the main shortcomings of the original Boussinesq models. Indeed research has been focused on extending the applicability of such models in the region characterized by deeper waters (Witting, 1984; Madsen et al., 1991; Nwogu, 1993; Gobbi and Kirby, 1999), by improving their dispersive characteristics. Some work has also been done to remove the original weakly nonlinear hypothesis, i.e. that the nonlinear effects exactly balance the dispersive ones, in order to get a better prediction of the highly nonlinear characteristics of the waves as they approach the breaking and also to further take advantage of the improved dispersive characteristics of the extended Boussinesq models at higher frequencies, as pointed out by Wei et al. (1995).

The main shortcoming of these models within the surf zone is the way in which they represent the energy dissipation due to breaking.

Different approaches have been proposed for this process, such as the eddy viscosity model of Zelt (1991), further developed by Kennedy et al. (2000), or the $k-\epsilon$ model of (Karambas and Koutitas, 1992), or the simplified roller approach of (Schäffer et al., 1993), improved recently by Veeramony and Svendsen (2000) and by Karambas and Tozer (2003). In particular, noticing that one of the most significant dissipative features of the flow within the surf zone is the presence of a large amount of breaking generated vorticity, Veeramony and Svendsen (2000) derived a weakly nonlinear Boussinesq model where the unrealistic hypothesis of irrotational flow has been removed. Instead, in Veeramony and Svendsen (2000), the dissipation terms due to breaking are derived as consequence of the presence of vorticity injected from the roller region within the flow.

Here, starting from the above mentioned work of Veeramony and Svendsen (2000), a fully nonlinear Boussinesq model has been derived. Such an extension is aimed at providing a better representation of the flow within the surf zone through a better description of the nonlinear properties of wave motion at breaking. Moreover a new numerical strategy of solution is implemented in order to better represent the breaking effects.

Comparisons with experimental literature data, considering regular and moderately irregular waves, will be presented and discussed to illustrate the actual improvements of the present model.

The paper is organized as follows: at first the derivation of the fully nonlinear continuity and momentum equations is presented, followed by the derivation of the analytical solution of the vorticity transport equation up to the same order as the governing equations. Then, the numerical procedure adopted to solve the problem is described, particularly focusing on the self-adaptive time varying grid approach. Then comparisons of the model results against both literature data and the weakly nonlinear version of the model are discussed. Finally, the problems arising from the modelling of breaking waves through a Boussinesq model are analyzed, such as the choice of the breaking criterion and the estimate of the dynamics of both the vorticity and, in turn, the breaking terms.

2. Description of the problem and mathematical formulation

Nearshore phenomena are characterized by a high degree of complexity, as simply sketched in Fig. 1 which, though complex, represents the physical processes involved therein in a very schematic way. Therefore, in order to describe the hydrodynamics of the surf zone through an analytical approach, several limiting assumptions have to be introduced. Here, the hypotheses used by Veeramony and Svendsen (2000) have been mainly maintained; thus, the Boussinesq equations are derived for waves propagating on relatively shallow waters, over a fixed bottom characterized by a gentle slope.

A sketch of both the physical problem analyzed and the main relevant variables along with the adopted reference system is shown in Fig. 2.

We use the long wave assumption to get the dimensionless mathematical formulation of the problem. For the horizontal coordinates x , the vertical coordinate z and for the time t , the following relevant scales are assumed (the hat sign indicates the dimensional variable):

$$x = k_0 \hat{x}; \quad z = \frac{\hat{z}}{h_0}; \quad t = k_0 \sqrt{gh_0} \hat{t} \quad (1)$$

where k_0 is a reference wave number, h_0 a reference water depth, a_0 a measure of the wave amplitude and g the gravity. The surface elevation ζ and the

stream function ψ are made dimensionless as follows

$$\zeta = \frac{\hat{\zeta}}{a_0}; \quad \psi = \frac{\hat{\psi}}{a_0 \sqrt{gh_0}} \quad (2)$$

The scaling of the dependent variables, e.g. the horizontal and vertical velocities u and w , follows from the previous scaling.

It turns out that the two dimensionless parameters, usually adopted for shallow water waves, namely the dispersive parameter and the nonlinear parameter, expressed respectively as

$$\mu = k_0 h_0 \text{ and } \delta = \frac{a_0}{h_0} \quad (3)$$

may be used also here to make estimates of the terms in the governing equations. Indeed, the shallow water assumption implies that $O(\mu^2) \ll O(1)$. If we assume weakly nonlinear waves, it implies that $O(\delta) < O(1)$.

Therefore it is consistent to neglect all terms of $O(\delta\mu^2)$ or smaller, as it was done in Veeramony and Svendsen (2000).

However, the assumption of weak nonlinearity represents a source of inaccuracy for the model, particularly close to the breaking point. Therefore in the following no assumptions are made about the order of magnitude of the nonlinear parameter δ , and the resulting model is fully nonlinear to terms of $O(\mu^2)$. As in Veeramony and Svendsen (2000), it is here assumed that the flow can be treated as irrotational only outside the surf zone, that is, the breaking

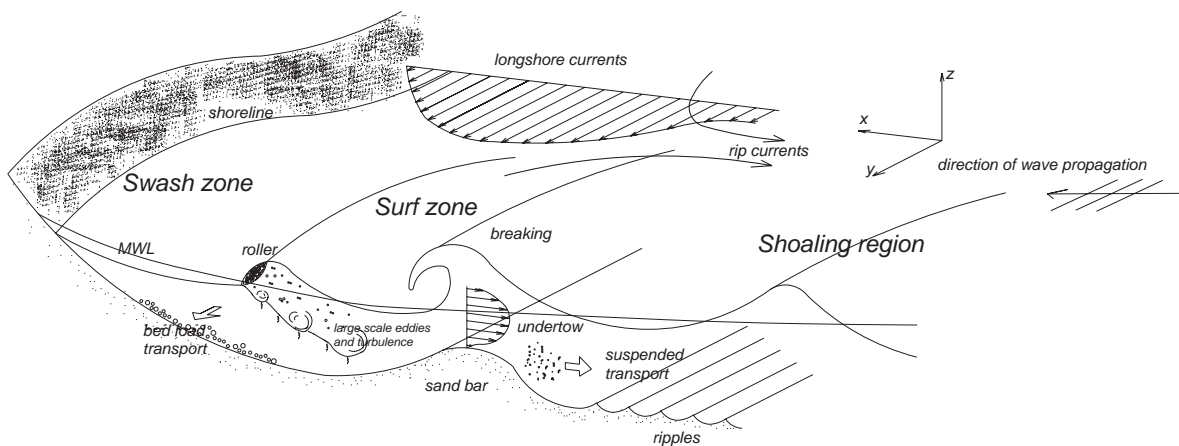


Fig. 1. Sketch of the complex surf zone hydrodynamics which typically occurs on gentle sloping beaches.

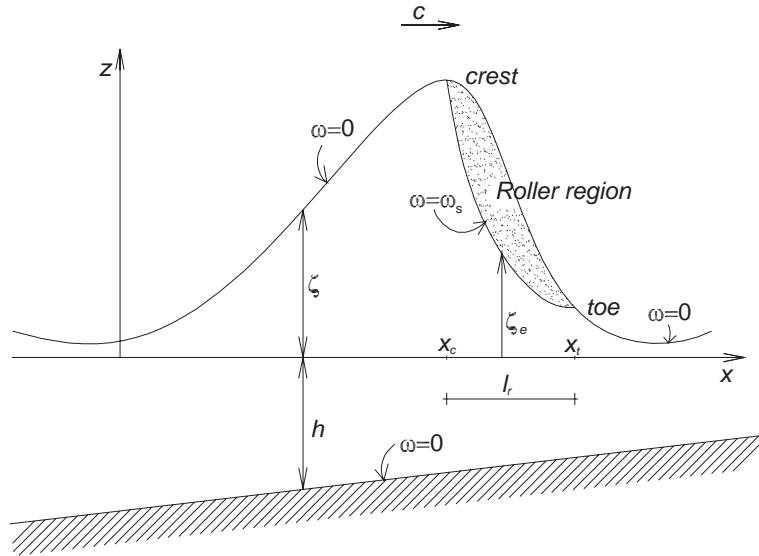


Fig. 2. Sketch of the adopted reference system and of the main variables. The boundary conditions on the vorticity ω after breaking are also represented.

is assumed to be the unique phenomenon which produces vorticity within the flow.

From the aforementioned variable scaling, the vorticity ω due to breaking scales as follows:

$$\omega = \frac{\partial u}{\partial z} - \mu^2 \frac{\partial w}{\partial x} = \frac{h_0}{\delta \sqrt{g h_0}} \hat{\omega} \quad (4)$$

On the basis of the previous relation it follows that when the flow can be assumed irrotational (i.e. $\omega=0$), the horizontal velocity is almost constant over the depth. Indeed Eq. (4) gives $\partial u/\partial z \sim O(\mu^2)$, while within the surf zone, i.e. in presence of a rotational motion, it is reasonable to assume $\omega \sim O(1)$. Thus a strong vertical variation of u , particularly close to the wave crest, is expected.

It is worth pointing out that while Veeramony and Svendsen (2000) used a $\zeta - Q$ formulation of the governing equations (Q being the volume flux), we here use a $\zeta - \bar{u}$ formulation. The depth averaged velocity \bar{u} is related to Q through the following relation

$$\bar{u} = \frac{Q}{h + \delta \zeta}. \quad (5)$$

As shown in the following, by this choice the equations can be written in a much simpler form.

2.1. Continuity and momentum equations

With reference to the system shown in Fig. 2, the depth integrated continuity equation, in non-dimensional form, reads

$$\frac{\partial \zeta}{\partial t} + \frac{\partial}{\partial x} [\bar{u} (h + \delta \zeta)] = 0 \quad (6)$$

which is exact, since no approximations have been introduced in order to obtain it.

The momentum equation is derived from the horizontal Reynolds equation by integrating over the depth and by applying the bottom and surface kinematic boundary conditions

$$\begin{aligned} \frac{\partial}{\partial t} \int_{-\hat{h}}^{\hat{\zeta}} \hat{u} d\hat{z} + \frac{\partial}{\partial \hat{x}} \int_{-\hat{h}}^{\hat{\zeta}} \hat{u}^2 d\hat{z} \\ = \frac{1}{\rho} \hat{p} (-\hat{h}) \frac{\partial \hat{h}}{\partial \hat{x}} \\ + \frac{1}{\rho} \frac{\partial}{\partial \hat{x}} \int_{-\hat{h}}^{\hat{\zeta}} (-\hat{p} + \hat{\tau}_{xx}) d\hat{z} \\ + \hat{R}_x^S - \hat{\tau}_x^B \end{aligned} \quad (7)$$

where ρ is the density of the water, \hat{p} the pressure, $\hat{\tau}_{ij}$ the shear stresses, and \hat{R}_x^S and $\hat{\tau}_x^B$ the stress on the surface and on the bottom respectively. In Eq. (7), the last two terms represent the horizontal components of

the shear stresses on the free surface and at the bottom, respectively.

Since within the surf zone the bottom generated turbulence is, at least, one order of magnitude smaller than the turbulence due to breaking, it seems reasonable to neglect the effect of the bottom boundary layer. Thus, at the bottom, a free slip boundary condition is applied, and it is assumed that the bottom shear stresses are negligible.

Indeed, while the bottom shear stress has a strong cumulative effect on waves propagating over long distances, the local effect is minimal and inside the surf zone the dissipation due to breaking dominates completely.

Moreover, by considering the similarity between surf zone waves and hydraulic jumps, it can be assumed that the normal stresses in the x direction, τ_{xx} are negligible. Indeed Svendsen et al. (2000) showed detailed measurements under the roller of the hydraulic jump, demonstrating that the effects of the turbulent stresses are only about 1% of the total momentum.

Finally, for simplicity we also neglect the wind stress, \hat{R}_x^S .

With these simplifications Eq. (7) reduces to:

$$\begin{aligned} \frac{\partial}{\partial \hat{t}} \int_{-\hat{h}}^{\hat{\zeta}} \hat{u} d\hat{z} + \frac{\partial}{\partial \hat{x}} \int_{-\hat{h}}^{\hat{\zeta}} \hat{u}^2 d\hat{z} \\ = \frac{1}{\rho} \hat{p} (-\hat{h}) \frac{\partial \hat{h}}{\partial \hat{x}} - \frac{1}{\rho} \frac{\partial}{\partial \hat{x}} \int_{-\hat{h}}^{\hat{\zeta}} \hat{p} d\hat{z} \end{aligned} \quad (8)$$

In order to eliminate the pressure from this equation, an expression for \hat{p} is derived by integrating between \hat{z} and $\hat{\zeta}$ the vertical momentum equation and by neglecting the stresses on the surface

$$\begin{aligned} \frac{\hat{p}(\hat{z})}{\rho} = g(\hat{\zeta} - \hat{z}) - \hat{w}^2 + \frac{\partial}{\partial \hat{t}} \int_{\hat{z}}^{\hat{\zeta}} \hat{w} d\hat{z} \\ + \frac{\partial}{\partial \hat{x}} \int_{\hat{z}}^{\hat{\zeta}} \left(\hat{u}\hat{w} - \frac{\hat{\tau}_{xz}}{\rho} \right) d\hat{z} \end{aligned} \quad (9)$$

The above expression indicates that the pressure is due to a hydrostatic contribution, as it is assumed in the nonlinear shallow water equations, with a non-hydrostatic contribution due to the vertical fluid motion, i.e. to the vertical acceleration and to the action of the adjacent water columns, which contribute to supporting the weight of the water.

An eddy viscosity ν_t is used to model the turbulent shear stress τ_{xz} . Such an eddy viscosity ν_t can be scaled as a function of a turbulence length scale and a velocity scale. Therefore, it can be written

$$\hat{\nu}_t \approx C_v \hat{h} \sqrt{g\hat{h}} \quad (10)$$

where C_v is assumed constant, experimentally calibrated, and taken in the range 0.01–0.03.

This is similar to Veeramony and Svendsen (2000) but clearly a crude formulation, since it does not take into account the vertical structure of the turbulence. It can also be discussed whether the horizontal variation of the turbulence is entirely controlled by the water depth, as Eq. (10) indicates. An alternative which may seem physically attractive would be to link ν_t to the energy dissipation as done e.g. by De Vriend and Stive (1987). However the energy dissipation due to breaking is not a parameter that is readily available from the solution of the governing equations and have to be estimated by using some model, for example assuming the similarity between breaking waves and hydraulic jumps and using a bore-like formulation or solving the transport equation for the depth averaged turbulent kinetic energy, as done by Karambas and Tozer (2003).

The scaling for $\hat{\nu}_t$ is then

$$\hat{\nu}_t = \mu h_0 \sqrt{g h_0} \nu_t \quad (11)$$

and the dimensionless shear stress $\hat{\tau}_{xz}$ and the total pressure result respectively

$$\hat{\tau}_{xz} = \delta \mu \rho g h_0 \nu_t \left(\frac{\partial u}{\partial z} + \mu^2 \frac{\partial w}{\partial x} \right) \quad (12)$$

$$\begin{aligned} p(z) = \left(\zeta - \frac{z}{\delta} \right) - \delta \mu^2 w^2 + \mu^2 \frac{\partial}{\partial \hat{t}} \int_z^{\delta \zeta} w dz \\ + \delta \mu^2 \frac{\partial}{\partial x} \int_z^{\delta \zeta} u w dz \\ - \mu^2 \frac{\partial}{\partial x} \int_z^{\delta \zeta} \nu_t \frac{\partial u}{\partial z} dz + O(\mu^4). \end{aligned} \quad (13)$$

Here the last term, which was not included in Veeramony and Svendsen (2000), accounts for the shear stresses within the fluid, which cannot be neglected inside regions with strong vorticity, i.e. in

the surf zone. Thus, the combined dimensionless momentum equation reads

$$\begin{aligned}
& \frac{\partial}{\partial t} \int_{-h}^{\delta\zeta} u dz + \delta \frac{\partial}{\partial x} \int_{-h}^{\delta\zeta} u^2 dz + (h + \delta\zeta) \zeta_x \\
& - \mu^2 \int_{-h}^{\delta\zeta} \frac{\partial^2}{\partial x \partial t} \int_z^{\delta\zeta} \frac{\partial}{\partial x} \int_{-h}^z u dz dz dz \\
& - \delta \mu^2 \int_{-h}^{\delta\zeta} \frac{\partial}{\partial x} \left(\frac{\partial}{\partial x} \int_{-h}^z u dz \right)^2 dz \\
& - \mu^2 \int_{-h}^{\delta\zeta} \frac{\partial^2}{\partial x^2} \int_z^{\delta\zeta} v_t \frac{\partial u}{\partial z} dz dz \\
& - \delta \mu^2 \int_{-h}^{\delta\zeta} \frac{\partial^2}{\partial x^2} \int_z^{\delta\zeta} u \frac{\partial}{\partial x} \int_{-h}^z u dz dz dz \\
& = O(\mu^4)
\end{aligned} \quad (14)$$

In order to evaluate the integrals in Eq. (14) and obtain a Boussinesq formulation for the equations, a velocity profile must be specified. The procedure proposed by [Veeramony and Svendsen \(2000\)](#) allows for the rotationality of the flow to be retained, and is adopted also here. Starting from the expression of the vorticity ω in terms of the stream function ψ

$$\mu^2 \psi_{xx} + \psi_{zz} = \omega \quad (15)$$

with the following boundary conditions

$$\psi(-h) = 0 \quad (16)$$

$$\psi(\delta\zeta) = \int_{-h}^{\delta\zeta} u dz. \quad (17)$$

By integrating Eq. (15), it turns out that the horizontal velocity is given by:

$$\begin{aligned}
u &= u_b - \mu^2 [2u_{bx}h_x + u_b h_{xx}] (z+h) - \frac{\mu^2}{2} u_{bxx} (z+h)^2 \\
& + \int_{-h}^z \omega dz - \mu^2 \int_{-h}^z \int_{-h}^z \int_{-h}^z \omega_{xx} dz dz dz + O(\mu^4)
\end{aligned} \quad (18)$$

where u_b is the horizontal velocity at the bottom.

This previous expression can be seen as composed of two components:

$$u = u_p + u_r \quad (19)$$

where the first term is a contribution similar to the velocity u_p in classical potential flow formulation of the Boussinesq model,

$$\begin{aligned}
u_p &= u_b - \mu^2 [2u_{bx}h_x + u_b h_{xx}] (z+h) \\
& - \frac{\mu^2}{2} u_{bxx} (z+h)^2 + O(\mu^4)
\end{aligned} \quad (20)$$

The second term is a contribution representing the vorticity ω , which can be thus called *rotational velocity* u_r

$$u_r = \int_{-h}^z \omega dz - \mu^2 \int_{-h}^z \int_{-h}^z \int_{-h}^z \omega_{xx} dz dz dz + O(\mu^4) \quad (21)$$

By averaging over the water column Eq. (20), the expression of the velocity at the bottom u_b can be derived in terms of the depth averaged velocity \bar{u}_p . By retaining terms only up to $O(\mu^2)$, it is possible to eliminate the dependency on u_b in Eq. (20) and after some algebra the total velocity u may be written as a function of both the depth averaged potential velocity \bar{u}_p and the rotational velocity u_r

$$\begin{aligned}
u &= \bar{u}_p + \mu^2 \left(h \bar{u}_p \right)_{xx} \left(\frac{\Delta_1}{2} - z \right) \\
& + \frac{\mu^2}{2} \bar{u}_{pxx} \left(\frac{\Delta_2}{3} - z^2 \right) + u_r + O(\mu^4)
\end{aligned} \quad (22)$$

where $\Delta_1 = \delta\zeta - h$ and $\Delta_2 = \delta^2 \zeta^2 - \delta\zeta h + h^2$.

The expression (22) for the total velocity differs from that found by [Veeramony and Svendsen \(2000\)](#), since here the nonlinear terms of $O(\delta, \delta^2)$ have been retained.

The fully nonlinear model is then obtained by substituting Eq. (22) into Eq. (14)

$$\begin{aligned}
& \bar{u}_t + \delta \bar{u}_{xt} + \zeta_x + \mu^2 \\
& \times \left[\left(B - \frac{1}{3} \right) h^2 \bar{u}_{xxt} - \frac{1}{2} h h_{xx} \bar{u}_t - h h_x \bar{u}_{xt} \right] \\
& + B \mu^2 h^2 \zeta_{xxx} + \delta \mu^2 \left[-\frac{1}{3} h^2 \bar{u}_{xxx} - h \zeta_x \bar{u}_{xt} \right. \\
& + \frac{1}{3} h^2 \bar{u}_x \bar{u}_{xx} - \frac{2}{3} h \zeta_x \bar{u}_{xt} - \frac{3}{2} h h_{xx} \bar{u}_x - \frac{1}{2} h h_{xx} \bar{u}^2 \\
& - h h_x \bar{u}_{xx} - \zeta h_x \bar{u}_{xt} - h_x \zeta_x \bar{u}_t - \frac{1}{2} \zeta h_{xx} \bar{u}_t \\
& \left. + B h^2 (\bar{u}_t)_{xx} \right] + \delta^2 \mu^2 \left[\frac{1}{6} \zeta^2 \bar{u}_{xxt} - \frac{1}{3} h \zeta_x \bar{u}_{xx} \right.
\end{aligned}$$

$$\begin{aligned}
 & -\frac{1}{3}h\bar{u}_{xx}(\zeta\bar{u})_x + h(\zeta\bar{u}_x^2)_x - \frac{1}{2}(\zeta^2\bar{u}_{xt})_x \\
 & -\frac{2}{3}h(\zeta\bar{u}\bar{u}_{xx})_x - \zeta_x h_{xx}\bar{u}^2 - \zeta h_x\bar{u}\bar{u}_{xx} \\
 & -\frac{1}{2}\zeta h_{xxx}\bar{u}^2 - \frac{3}{2}\zeta h_{xx}\bar{u}\bar{u}_x - \zeta_x h_x\bar{u}\bar{u}_x \Big] \\
 & + \delta^3\mu^2 \left[-\frac{1}{3}\zeta^2\bar{u}\bar{u}_{xxx} - \zeta\zeta_x\bar{u}\bar{u}_{xx} + \zeta\zeta_x\bar{u}_x^2 \right. \\
 & \left. + \frac{1}{3}\zeta^2\bar{u}_x\bar{u}_{xx} \right] + [\delta(\Delta M)_x + \mu^2(\Delta P)_{xxt} - \mu^2 D_s \\
 & + \delta\mu^2(\Delta M_1)_x + \delta\mu^2 D_w + \delta\mu^2 D_{uw}] (h + \delta\zeta)^{-1} \\
 & = O(\mu^4) \tag{23}
 \end{aligned}$$

In order to enhance the dispersion characteristics of the model in deeper water the linear operator $\mathcal{L} = 1 + B\mu^2 h^2 \nabla^2$, with $B=1/15$ suggested by Maden and Schäffer (1998) has been applied.

The weakly nonlinear model of Veeramony and Svendsen (2000) can be recovered from Eq. (23) by assuming $O(\delta)=O(\mu^2)$ and by neglecting both terms smaller than $O(\mu^2)$ and the term $\mu^2 D_s$ which was not included in Veeramony and Svendsen (2000).

It is worth pointing out that due to the absence of restrictions on the order of magnitude of δ , the traditional Boussinesq approximation, which postulates the balance between the dispersive and nonlinear effects, is no longer valid. This allows for a better modelling of the flow close to the breaking point and inside the surf zone where the waves show highly nonlinear characteristics.

It must be also noticed that the terms $(\Delta M)_x$, $(\Delta P)_{xxt}$, $(\Delta M_1)_x$, D_w , D_s and D_{uw} are all functions of the rotational velocity u_r , which, in turn, depends on the vorticity ω injected inside the flow by the breaking mechanism. Thus, the aforementioned terms are called *breaking terms*, as they represent the excess of momentum flux (i.e. the dissipation of energy) due to breaking.

In particular, D_s is the shear stress inside the fluid. If we assume the eddy viscosity ν_t constant over depth D_s can be written

$$\begin{aligned}
 D_s = & (h + \delta\zeta)[\nu_t u_r(\delta\zeta)]_{xx} + \delta\zeta_x[\nu_t u_r(\delta\zeta)]_x \\
 & + \delta[\nu_t u_r(\delta\zeta)\zeta_x] - [\nu_t \bar{u}_r(h + \delta\zeta)]_{xx} \tag{24}
 \end{aligned}$$

The terms

$$(\Delta M)_x = \frac{\partial}{\partial x} \int_h^{\delta\zeta} (u_r^2 - \bar{u}_r^2) dz \tag{25}$$

and

$$\begin{aligned}
 (\Delta M_1)_x & = \frac{\partial}{\partial x} \left[-\bar{u}_{pxx} \int_{-h}^{\delta\zeta} (2hz + z^2)(u_r - \bar{u}_r) dz + O(h_x) \right] \\
 & \tag{26}
 \end{aligned}$$

give the excess of momentum flux due to the vertical variation of the rotational velocity along the water column. The term

$$\begin{aligned}
 (\Delta P)_{xxt} = & \frac{\partial}{\partial x} \frac{\partial}{\partial x} \frac{\partial}{\partial t} \left[-\int_{-h}^{\delta\zeta} \int_z^{\delta\zeta} \int_{-h}^z (u_r - \bar{u}_r) dz dz dz \right] \\
 & \tag{27}
 \end{aligned}$$

is the contribution to the pressure due to the vertical motion (the minus sign was missing in Veeramony and Svendsen, 2000). Finally,

$$\begin{aligned}
 D_w = & \int_{-h}^{\delta\zeta} \frac{\partial}{\partial x} \left[\left(\frac{\partial}{\partial x} \int_{-h}^z (u_r - \bar{u}_r) dz \right) \right. \\
 & \left. \times \left(\frac{\partial}{\partial x} \int_{-h}^z (2\bar{u} + u_r - \bar{u}_r) dz \right) \right] dz \tag{28}
 \end{aligned}$$

is the excess of momentum due to the vertical motion and

$$\begin{aligned}
 D_{uw} = & \int_{-h}^{\delta\zeta} \frac{\partial^2}{\partial x^2} \int_z^{\delta\zeta} \left[(u_r - \bar{u}_r) \frac{\partial}{\partial x} \int_{-h}^z \bar{u} dz \right. \\
 & \left. + (\bar{u} + u_r - \bar{u}_r) \frac{\partial}{\partial x} \int_{-h}^z (u_r - \bar{u}_r) dz \right] dz dz \tag{29}
 \end{aligned}$$

represents the stresses exerted on the vertical column by the adjacent columns of fluid.

2.2. Vorticity transport equation

The mechanism of vorticity generation near the free surface is still to be established firmly. Several theories have been proposed which attribute the

breaker generated vorticity to the pressure gradient or to the density gradient close to the overturning roller (Lin and Rockwell, 1995; Nadaoka et al., 1989; Melville et al., 2002).

Here we assume, following Veeramony and Svendsen (2000), that the vorticity is generated primarily in the roller from where it spreads downwards by diffusion and convection due to turbulence. By using this approach, the breaking strongly influences the flow through the rotational velocity u_r . In order to determine such a velocity the vorticity transport equation has to be integrated along with the governing equations. In dimensionless form the vorticity equation reads:

$$\frac{\partial \omega}{\partial t} + \delta u \frac{\partial \omega}{\partial x} + \delta w \frac{\partial \omega}{\partial z} = v_t \left(\mu^2 \frac{\partial^2 \omega}{\partial x^2} + \frac{\partial^2 \omega}{\partial z^2} \right) \quad (30)$$

Eq. (30) is able to model the transport of vorticity inside the flow, but an appropriate source of vorticity must be also included. Here the source of vorticity is schematized through the roller approach. In particular, it is assumed that the main source of vorticity is located on the lower edge of the roller, such an assumption is qualitatively confirmed by the experimental results of Lin (1994). Indeed this author, by analyzing the instantaneous structure of a stationary breaking wave, shows that the discontinuous slope of the free surface and the occurrence of the separation beneath the surface represent a powerful source of vorticity, as a mixing layer is formed behind the toe of the roller. However, it is useful to stress that the surface roller concept does not correspond to a detailed representation of the flow, but only to a useful macroscopic schematization of it.

According to the above considerations, the source of vorticity is retained at the lower edge of the surface roller and the boundary and initial conditions for Eq. (30) can be written as follows

$$\omega(x, z = \delta \zeta, t) = \omega_s \quad (31)$$

$$\omega(x, z = -h, t) = 0 \quad (32)$$

$$\omega(x, z, t = 0) = 0 \quad (33)$$

Veeramony and Svendsen (2000) proposed an analytical solution of Eq. (30), since a numerical solution would have required a heavy computational effort.

Moreover in very shallow waters the vertical grid size required to get a sufficiently accurate description should be very fine, leading to very small time steps to obtain the numerical stability of the model. Here the analytical approach used by Veeramony and Svendsen (2000) is extended up to $O(\delta)$, consistently with the order of the Boussinesq equations.

In order to get the analytical solution, the physical coordinates (x, z, t) are changed to the computational coordinates (x, σ, t) , which are defined as

$$\sigma = \frac{h + z}{h + \delta \zeta_e} \quad (34)$$

so that the computational domain is changed from $-h \leq z \leq \zeta_e$ to $0 \leq \sigma \leq 1$. In this way the irregular physical domain is transformed into a regular rectangular computational domain.

Neglecting terms of $O(\mu^2)$ the vorticity transport equation in the new reference system becomes

$$\begin{aligned} \frac{\partial \omega}{\partial t} - \delta \left[\frac{\sigma}{h + \delta \zeta_e} \frac{\partial \zeta_e}{\partial t} \right] \frac{\partial \omega}{\partial \sigma} + \delta u \frac{\partial \omega}{\partial x} - \delta^2 \frac{u \sigma}{h + \delta \zeta_e} \\ \times \frac{\partial \zeta_e}{\partial x} \frac{\partial \omega}{\partial \sigma} + \delta \left[\frac{w}{h + \delta \zeta_e} \right] \frac{\partial \omega}{\partial \sigma} = \frac{v_t}{(h + \delta \zeta_e)^2} \frac{\partial^2 \omega}{\partial \sigma^2} \\ + O(\mu^2, \delta h_x) \end{aligned} \quad (35)$$

while the boundary and the initial conditions can be rewritten as follows

$$\omega(x, \sigma = 1, t) = \omega_s(x, t) \quad (36)$$

$$\omega(x, \sigma = 0, t) = 0 \quad (37)$$

$$\omega(x, \sigma, t = 0) = 0 \quad (38)$$

By applying the variable change

$$\omega = \Omega + \sigma \omega_s \quad (39)$$

the boundary conditions become homogeneous and the problem can be handled more easily. We then have the boundary conditions

$$\Omega(x, \sigma = 1, t) = 0 \quad (40)$$

$$\Omega(x, \sigma = 0, t) = 0 \quad (41)$$

$$\Omega(x, \sigma, t = 0) = 0 \quad (42)$$

To solve Eq. (39), a perturbation method is used. It is assumed that Ω can be expanded in terms of the small parameter δ as

$$\Omega = \omega^{(1)} + \delta\omega^{(2)} + \delta^2\omega^{(3)} + O(\delta^3) \quad (43)$$

By expanding also the following term in a Taylor series

$$\frac{v_t}{(h + \delta\zeta_e)^2} = \frac{v_t}{h^2} \left[1 - 2\delta\frac{\zeta_e}{h} + O(\delta^2) \right] \quad (44)$$

the vorticity transport equation finally reads

$$\begin{aligned} \frac{\partial\omega^{(1)}}{\partial t} + \delta\frac{\partial\omega^{(2)}}{\partial t} + \sigma\frac{\partial\omega_s}{\partial t} - \delta\frac{\omega_s\sigma}{h + \delta\zeta_e}\frac{\partial\zeta_e}{\partial t} \\ - \delta\left[\frac{\sigma}{h + \delta\zeta_e}\frac{\partial\zeta_e}{\partial t} - \frac{w}{h + \delta\zeta_e} \right] \\ \times \left(\frac{\partial\omega^{(1)}}{\partial\sigma} + \delta\frac{\partial\omega^{(2)}}{\partial\sigma} + \omega_s \right) \\ + \delta u\frac{\partial\omega^{(1)}}{\partial x} + \delta u\sigma\frac{\partial\omega_s}{\partial x} = \frac{v_t}{h^2} \left(1 - 2\delta\frac{\zeta_e}{h} \right) \\ \times \left(\frac{\partial^2\omega^{(1)}}{\partial\sigma^2} + \delta\frac{\partial^2\omega^{(2)}}{\partial\sigma^2} \right) + O(\delta^3) \end{aligned} \quad (45)$$

Eq. (45) must be solved up to $O(\delta)$, consistently with the momentum equation where only terms larger than $O(\delta)$ do appear.

In the following the analytical derivation of the $O(1)$ and at $O(\delta)$ terms will be presented.

2.2.1. $O(1)$: basic state

The procedure to obtain the solution of the basic state $O(1)$ is similar to the one used by Veeramony and Svendsen (2000), however here it is reported for the sake of completeness. The problem at $O(1)$ reads

$$\frac{\partial\omega^{(1)}}{\partial t} - \kappa\frac{\partial^2\omega^{(1)}}{\partial\sigma^2} = -\sigma\frac{\partial\omega_s}{\partial t} \quad (46)$$

with

$$\kappa = \frac{v_t}{h^2} \quad (47)$$

Eq. (46) has to be solved along with the boundary conditions

$$\omega^{(1)}(\sigma = 1, t) = 0 \quad (48)$$

$$\omega^{(1)}(\sigma = 0, t) = 0 \quad (49)$$

$$\omega^{(1)}(\sigma, t = 0) = 0 \quad (50)$$

The right hand side of Eq. (46) is an odd function in σ , then it can be expanded as half-sine Fourier series

$$-\sigma\frac{\partial\omega_s}{\partial t} = \sum_{n=1}^{\infty} F_n^{(1)} \sin n\pi\sigma \quad (51)$$

where, for each n , by definition the coefficients may be expressed as

$$\begin{aligned} F_n^{(1)} &= \int_{-1}^1 -\sigma\frac{\partial\omega_s}{\partial t} \sin n\pi\sigma \, d\sigma \\ &= -2\frac{\partial\omega_s}{\partial t} \int_0^1 \sigma \sin n\pi\sigma \, d\sigma \\ &= 2\frac{(-1)^n}{n\pi} \frac{\partial\omega_s}{\partial t} \end{aligned} \quad (52)$$

It is assumed that the solution has the form

$$\omega^{(1)} = \sum_{n=1}^{\infty} G_n^{(1)} \sin n\pi\sigma \quad (53)$$

where the coefficients of the series $G_n^{(1)}$ are only function of x and t . Substituting expressions (51) and (53) in Eq. (46) gives

$$\begin{aligned} \frac{\partial}{\partial t} \left[\sum_{n=1}^{\infty} G_n^{(1)} \sin n\pi\sigma \right] - \kappa\frac{\partial^2}{\partial\sigma^2} \left[\sum_{n=1}^{\infty} G_n^{(1)} \sin n\pi\sigma \right] \\ = \sum_{n=1}^{\infty} F_n^{(1)} \sin n\pi\sigma \end{aligned} \quad (54)$$

which becomes, after expanding the second term on the left hand side:

$$\sum_{n=1}^{\infty} \left[\frac{\partial G_n^{(1)}}{\partial t} + \kappa n^2 \pi^2 G_n^{(1)} - F_n^{(1)} \right] \sin n\pi\sigma = 0 \quad (55)$$

The last equation must be true for all the values of σ , then it has to be

$$\frac{\partial G_n^{(1)}}{\partial t} + \kappa n^2 \pi^2 G_n^{(1)} - F_n^{(1)} = 0 \quad (56)$$

This equation is a nonhomogeneous first order differential equation in $G_n^{(1)}$, which may be solved by using

the method of variation of parameters in order to get the following general solution

$$G_n^{(1)} = C e^{-\kappa n^2 \pi^2 t} + e^{-\kappa n^2 \pi^2 t} \int_0^t F_n^{(1)} e^{\kappa n^2 \pi^2 \tau} d\tau \quad (57)$$

where C is an integration constant which turns to be equal to 0, by using the initial condition.

The solution of the basic state is then given by the following coefficients

$$G_n^{(1)} = (-1)^n \frac{2}{n\pi} \int_0^t \frac{\partial \omega_s}{\partial t} e^{\kappa n^2 \pi^2 (\tau-t)} d\tau \quad (58)$$

This part of the solution coincides with the one obtained in [Veeramony and Svendsen \(2000\)](#). However, in the present fully nonlinear model also the $O(\delta)$ solution must be taken into account.

2.2.2. $O(\delta)$ perturbed state

Considering, now, the problem at $O(\delta)$, this gives rise to the following equation

$$\frac{\partial \omega^{(2)}}{\partial t} - \kappa \frac{\partial^2 \omega^{(2)}}{\partial \sigma^2} = F^{(2)} \quad (59)$$

with the following boundary and initial conditions

$$\omega^{(2)}(\sigma = 1, t) = 0 \quad (60)$$

$$\omega^{(2)}(\sigma = 0, t) = 0 \quad (61)$$

$$\omega^{(2)}(\sigma, t = 0) = 0 \quad (62)$$

and where the right hand side of Eq. (59) has been defined as

$$F^{(2)} = -2\kappa \frac{\zeta_e}{h} \frac{\partial^2 \omega^{(1)}}{\partial \sigma^2} + 2\omega_s \frac{\sigma}{h} \frac{\partial \zeta_e}{\partial t} + \frac{\sigma}{h} \frac{\partial \zeta_e}{\partial t} \frac{\partial \omega^{(1)}}{\partial \sigma} - u \frac{\partial \omega^{(1)}}{\partial x} - u\sigma \frac{\partial \omega_s}{\partial x} - \frac{w}{h} \left(\frac{\partial \omega^{(1)}}{\partial \sigma} + \omega_s \right) \quad (63)$$

after expanding the term $(h + \delta \zeta_e)^{-1}$ in Taylor series about zero.

The solution of the $O(1)$ problem, $\omega^{(1)}$, becomes the forcing for the problem to the next order of approximation. In analogy with the first case, also here, it is assumed that the solution has the form

$$\omega^{(2)} = \sum_{n=1}^{\infty} G_n^{(2)} \sin n\pi\sigma \quad (64)$$

Since Eq. (59) is similar to Eq. (46), following the same approach as before, the function F is expanded as half-range sinusoidal series

$$F^{(2)} = \sum_{n=1}^{\infty} F_n^{(2)} \sin n\pi\sigma \quad (65)$$

and the coefficients of this series can be calculated as

$$F_n^{(2)} = \int_{-1}^1 F^{(2)} \sin n\pi\sigma d\sigma = 2 \int_0^1 F^{(2)} \sin n\pi\sigma d\sigma \quad (66)$$

According to Eq. (64) the solution to Eq. (59) is then given by the following coefficients

$$G_n^{(2)} = \int_0^t F_n^{(2)} e^{\kappa n^2 \pi^2 (\tau-t)} d\tau \quad (67)$$

2.2.3. Complete solution

Finally, the total expression of the vorticity results

$$\omega = \sigma\omega_s + \sum_{n=1}^{\infty} [G_n^{(1)} + \delta G_n^{(2)}] \sin n\pi\sigma \quad (68)$$

Considering that the first term in Eq. (68) can also be written as

$$\sigma\omega_s = \sum_{n=1}^{\infty} G_n^{(0)} \sin n\pi\sigma \quad (69)$$

where $G_n^{(0)}$ is determined as

$$G_n^{(0)} = \int_{-1}^1 \sigma\omega_s \sin n\pi\sigma d\sigma = -2\omega_s \frac{(-1)^n}{n\pi} \quad (70)$$

more synthetically the solution for ω can be written as

$$\omega = \sum_{n=1}^{\infty} G_n \sin n\pi\sigma \quad (71)$$

where the coefficients G_n have been defined as

$$G_n = G_n^{(0)} + G_n^{(1)} + \delta G_n^{(2)} \quad (72)$$

It is useful to stress that Eq. (71) differs from the weakly nonlinear solution found by [Veeramony and Svendsen \(2000\)](#), since here, for consistency with the governing equations, the solution at $O(\delta)$ has been

also considered to get the solution of the vorticity transport equation.

The expressions for the rotational velocity and for the breaking terms can be derived by submitting Eq. (71) into Eq. (21) and Eqs. (24)–(29). The details are shown in Appendix A.

2.2.4. Similarity with the hydraulic jump

In order to specify the amount of vorticity injected within the flow by the breaking waves, the hydraulic similarity between the roller of a breaking wave and the turbulent region on the front of an hydraulic jump is assumed. Referring to the experimental investigation of three hydraulic jumps with Froude numbers similar to those of breaking waves performed by Svendsen et al. (2000), Veeramony and Svendsen (2000) used a best fit of experimental data in order to determine the roller thickness ζ_s and the vorticity at the lower edge of the roller ω_s . The expressions, corrected from the typos appeared in Veeramony and Svendsen (2000), are

$$\frac{\zeta_s}{h_2\sqrt{\xi}} = 0.78e^{-\frac{x'}{l_r}}\left(\frac{x'}{l_r} - \frac{x'^2}{l_r^2}\right) \quad (73)$$

$$\frac{\omega_s h_2 \xi}{U_1} = 15.75\left(1 - \frac{x'}{l_r}\right) \quad (74)$$

where h_1 and h_2 represent the minimum water depth before the jump and the undisturbed water depth downstream with respect to the jump, respectively, ξ is the ratio h_2/h_1 and U_1 is the velocity of the flow beneath the weir. When transferred to the case of a moving breaking wave, the coordinate $x' = -(x - x_t)$ is equivalent to a reference system moving at the same wave speed (see Fig. 3).

Concerning the estimate of ω_s , at the toe of the roller a ramping of Eq. (74), analogous to the one adopted by Veeramony and Svendsen (2000), has been used in the present model in order to facilitate the numerical computations.

3. Numerical solution

The numerical scheme used to solve Eqs. (6) and (23) is the Adams–Bashforth–Moulton. To highlight the numerical methods used to implement the boundary conditions, the computational schematization of the physical domain is shown in Fig. 4. In particular at the offshore boundary outgoing waves are allowed to leave the domain by using the absorbing–generating boundary condition introduced by Van Dongeren and Svendsen (1997), while at the onshore boundary a sponge layer has been used in order to dissipate the wave motion at the shoreward boundary of the domain.

It is worth pointing out that a widely adopted five points Shapiro filter has been used both in the Veeramony and Svendsen (2000) and in the present version of the model, particularly within the surf zone, in order to avoid spurious oscillations of the solution. Indeed the added numerical viscosity due to such a filter, though influences the overall dissipation, appears to be useful in order to obtain appropriate results, particularly regarding the free surface elevation.

In the present work, particular attention has been given at implementing the boundary conditions of the vorticity transport equation. Indeed, the key-point of the proposed procedure is the definition of the amount

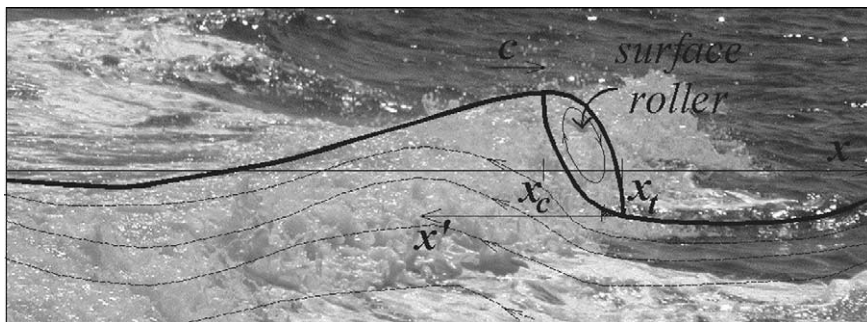


Fig. 3. Sketch of the local reference system adopted for a moving breaking wave in the numerical scheme.

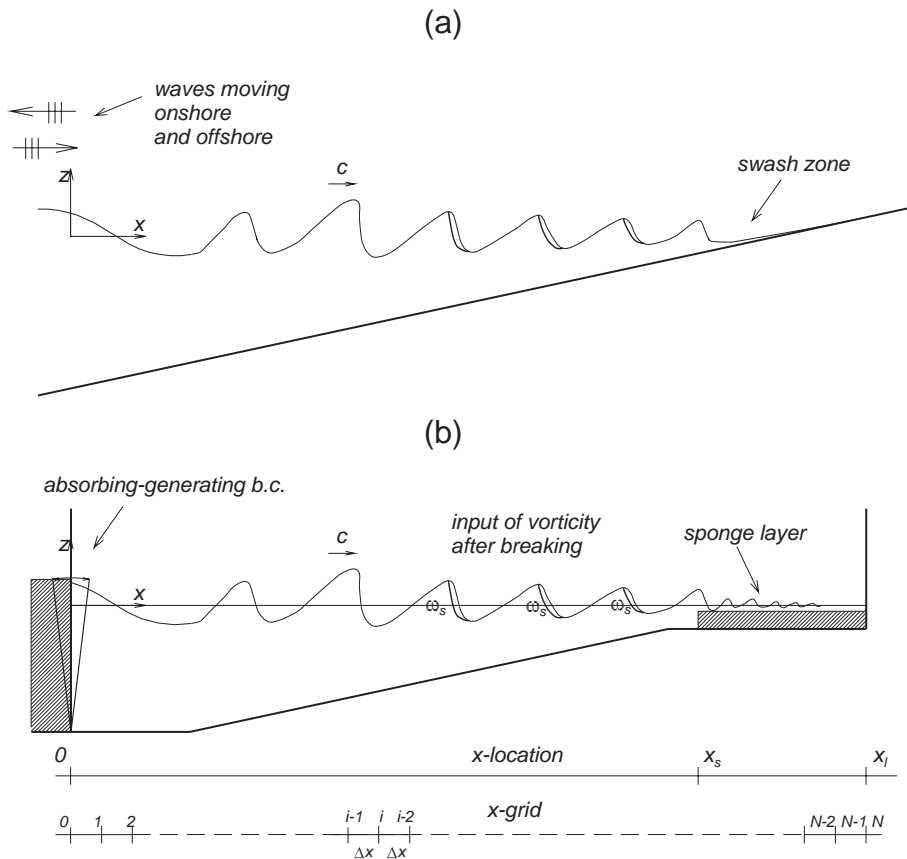


Fig. 4. a) Physical problem and b) adopted conceptual model along with the treatment of the offshore and onshore boundary conditions.

of vorticity at the lower edge of the roller. Fig. 5a shows that according to Eq. (74) at the surface there is a strong discontinuity of the vorticity close to the toe of the roller, as the vorticity suddenly increases as the toe of the breaking front passes a point where there is the breaking onset, there the maximum value of vorticity occurs very shortly. Such a discontinuity is obviously difficult to be treated accurately within a numerical model, and it has a tendency to generate strong instabilities. Moreover it turns out that the total energy dissipation in the wave depends strongly on the accuracy at this point. Therefore in order to describe the impulsive behavior of breaking waves a very high accuracy should be guaranteed right at the roller toe.

However, the roller region represent just a spatially limited portion of the overall computational domain. Outside this domain a rather coarse grid actually

suffices. Thus, from a numerical point of view, the use of an uniformly spaced computational grid to solve the governing equations results in a quite poor representation of the roller characteristics, since only few grid points fall within such a region.

Multi-grid methods have been developed to describe phenomena where a great accuracy is needed only locally, such as in a very irregular domain (Wu et al., 1997; Spitaleri and Corinaldesi, 1997; Kania, 1999; Papadakis and Bergeles, 1999; Park and Borthwick, 2001), while time-varying grids have been used in some cases to model phenomena quickly varying in time, but only in some part of the domain, such as the evolution of the front of the free surface profile due to a dam break (Lie et al., 1998; Jeong and Yang, 1998; Jeong and Yang, 1999; Jha et al., 2001). Unfortunately, these methods have often been coupled to Volume of Fluid (VOF) methods.

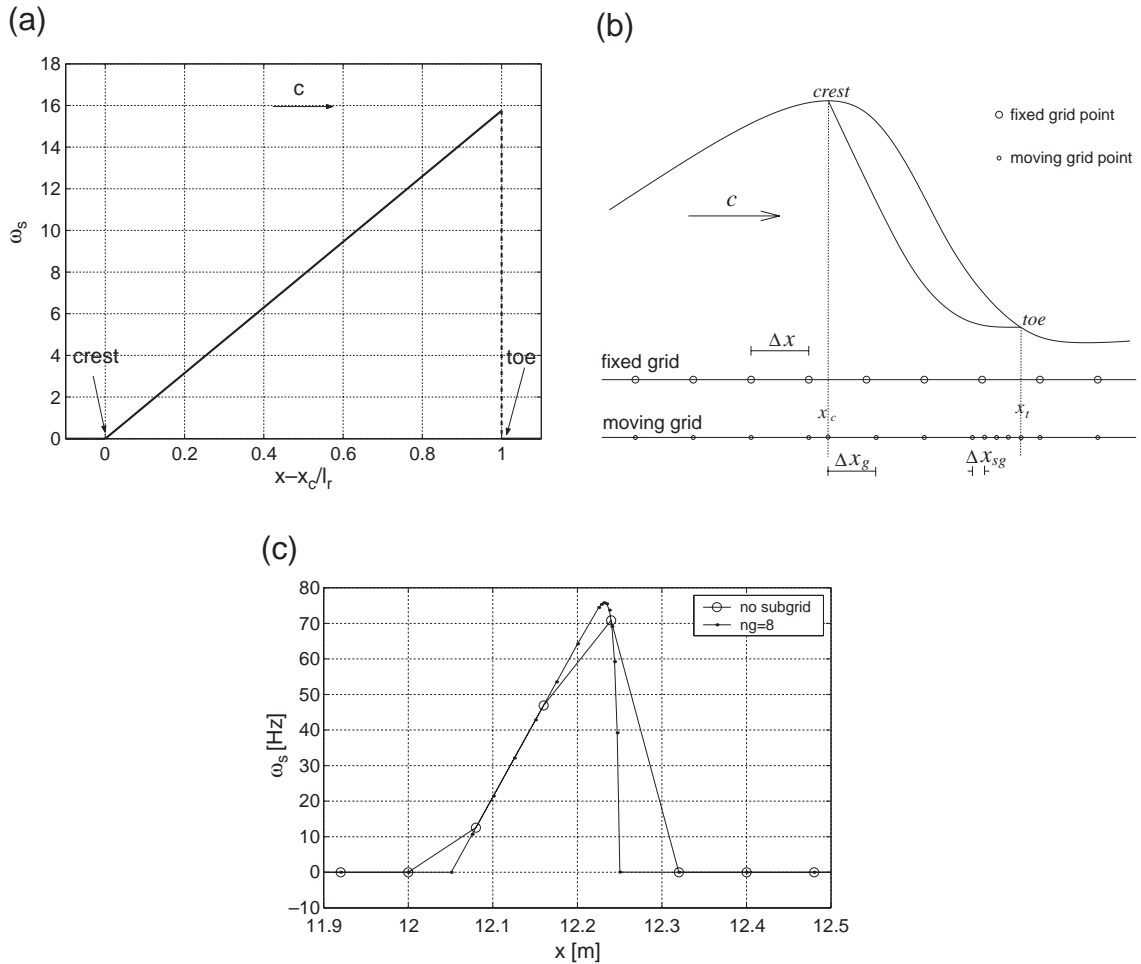


Fig. 5. (a) Experimental distribution of vorticity at the lower edge of the roller according to the similarity with the hydraulic jump; (b) sketch of the original self-adaptive time varying grid; (c) estimate of the vorticity distribution at the lower edge of the roller by means of the fixed uniform grid (circles) and by the moving varying one (dots).

Moreover, the grid needed here must also be time-varying, as the grid points should move with the waves. Therefore, also the celerity of the numerical cells should be estimated.

In this work an accurate description of the roller has been obtained by a new algorithm which implements a self-adaptive-time-varying grid. Such a grid is defined so that it is finer at the toe and is characterized by grid points which vary according to the actual dimension of the surface roller. Such a new numerical strategy provides a better resolution in the region where the vorticity is generated through the nested

subgrid, without heavily affecting the computational efficiency of the model.

The formulation used to define the proposed grid, represented in Fig. 5b, is the following

$$\Delta x_g = \frac{x_t - x_c}{ng}; \quad \Delta x_{sg} = \frac{\Delta x_g}{ng} \quad (75)$$

where Δx_g is the interval of the first gross subdivisions inside the roller region, x_t and x_c are the positions of the toe and of the crest respectively, ng is the fundamental number of subdivisions and Δx_{sg} is the interval of the finer subdivisions, located close to the toe.

The position x_g^i of a point inside the subgrid can then be defined as

$$x_g^i = x_g^{i-1} + \begin{cases} \Delta x_g, & x_c \leq x_g^{i-1} < x_t - \Delta x_g \\ \Delta x_{sg}, & x_t - \Delta x_g \leq x_g^{i-1} < x_t \end{cases} \quad (76)$$

It should be noticed that the number of representative points inside the roller is thus fixed, being equal to $2ng$, and independent from the length of the roller. Instead, the size of the subdivisions changes according to the roller dimensions, keeping always the same degree of accuracy inside the roller. Moreover, the subgrid moves following the roller evolution, while outside of the roller region the uniform grid spacing is kept.

Fig. 5c shows the difference in evaluating ω_s using the uniform fixed grid and using the subgrid, for $ng=8$, demonstrating how the subgrid approach catches better the impulsive increase of vorticity at the toe of the roller.

The analytical perturbation solution of the vorticity transport equation is then calculated onto the proposed self-adaptive time varying grid. In particular, it has been possible to overcome the aforementioned difficulties about the calculations of the time and space derivatives. The space derivatives were calculated onto the fixed uniform grid (i.e. where the variable to be derived are known from the solution of the Boussinesq equations) and then transferred by linear interpolation onto the actual moving irregular grid.

Since the grid is moving, the procedure to calculate the time derivatives is more complex. Let (x,t) be the real domain and (x^*,t^*) be the image domain

$$x \rightarrow x^* \quad (77)$$

$$t \rightarrow t^* \quad (78)$$

Being f a generic variable, the time derivatives should be evaluated, by using the chain rule, as

$$\begin{aligned} \frac{\partial f}{\partial t^*} \Big|_{x^*} &= \frac{\partial f}{\partial x} \Big|_t \frac{\partial x}{\partial t^*} \Big|_{x^*} + \frac{\partial f}{\partial t} \Big|_x \Rightarrow \\ \frac{\partial f}{\partial t} \Big|_x &= \frac{\partial f}{\partial t^*} \Big|_{x^*} - \frac{\partial f}{\partial x} \Big|_t \frac{\partial x}{\partial t^*} \Big|_{x^*} \end{aligned} \quad (79)$$

where it is assumed, as a first approximation, that

$$\frac{\partial x}{\partial t^*} \Big|_{x^*} \approx c \approx \sqrt{g(h+\zeta)} \quad (80)$$

However, this derivation is only valid if there is a perfect correspondence of the number of grid points between the real domain and the image domain, meaning that the grid number has to be the same in both cases. Unfortunately, this is not the case here, in fact the subgrid introduced in the previous section, has more points than the uniform grid, in order to increase the accuracy within the roller region. Moreover, since the roller moves and new rollers are generated inside the domain as the wave propagates, the number of points of the moving grid is not only greater than in the fixed grid, but it also varies in time.

Due to the aforementioned limit, a different procedure has been adopted in this work. In order to calculate the time derivatives, the old values of the variables have been stored and transferred, by linear interpolation, from the moving grid at the previous time step, n , onto the moving grid at the next time step, $n+1$. Then, the time derivatives are evaluated at the same point onto the current moving grid.

Comparisons of the time derivatives evaluated on the uniform fixed grid and on the moving self-adaptive grid showed that, due to the re-definition of the toe position and to the higher resolution obtained close to it, the method used here allows for a better prediction of the impulsive characteristics of the wave breaking flow.

4. Comparisons with literature data

In order to test the model performances, comparisons with experimental literature data have been performed both for regular waves and partly irregular waves (in the form of group waves). It is worth pointing out that while the comparison with regular wave data was aimed at estimating the improvement of this new model with respect to the weakly nonlinear version of [Veeramony and Svendsen \(2000\)](#), the comparison with wave groups was aimed at validating the predictive capabilities of the model not only with respect to the surface profile and wave heights, but also at verifying the effects of time and space varying wave breaking.

4.1. Regular waves

The comparison were conducted with the laboratory measurements by [Hansen and Svendsen \(1979\)](#),

for three different wave conditions (see Fig. 6). The objectives were to get an overall picture of the effects of the improvements due to the fully nonlinear characteristics of the model through its prediction of wave height distribution along the domain, which, in turn, represents an estimate of predictive goodness of the breaking generated dissipation.

At the beginning of the shoaling region the Veeramony and Svendsen (2000) model and the fully nonlinear model provide basically the same results, which are in very good agreement with the experimental data.

However, further onshore, just before the breaking point, the weakly nonlinear model performance compares poorly with the data: the weakly nonlinear Veeramony and Svendsen (2000) model overestimates the increase in wave height. These discrepancies are essentially eliminated in the fully nonlinear model.

The same result was found by Wei et al. (1995), who compared their fully nonlinear model with the weakly nonlinear one of Wei and Kirby (1995) and by Madsen et al. (2002).

Such a poor representation, right before the breaking point, strongly affects the characteristics of waves within the surf zone. It is also interesting to recall that in comparison traditional sinusoidal wave theory strongly underpredicts the wave height increase toward breaking.

Inside the surf zone, the fully nonlinear model agrees quite well with the experimental data, both in the transition region, characterized by higher gradient of wave height and in the inner surf zone. At the breaking point, however, there is a slight underprediction of the wave height value. Moreover, it may be worth noticing that the last test (Test Q) actually corresponds to plunging breaker conditions. At least in principle, no

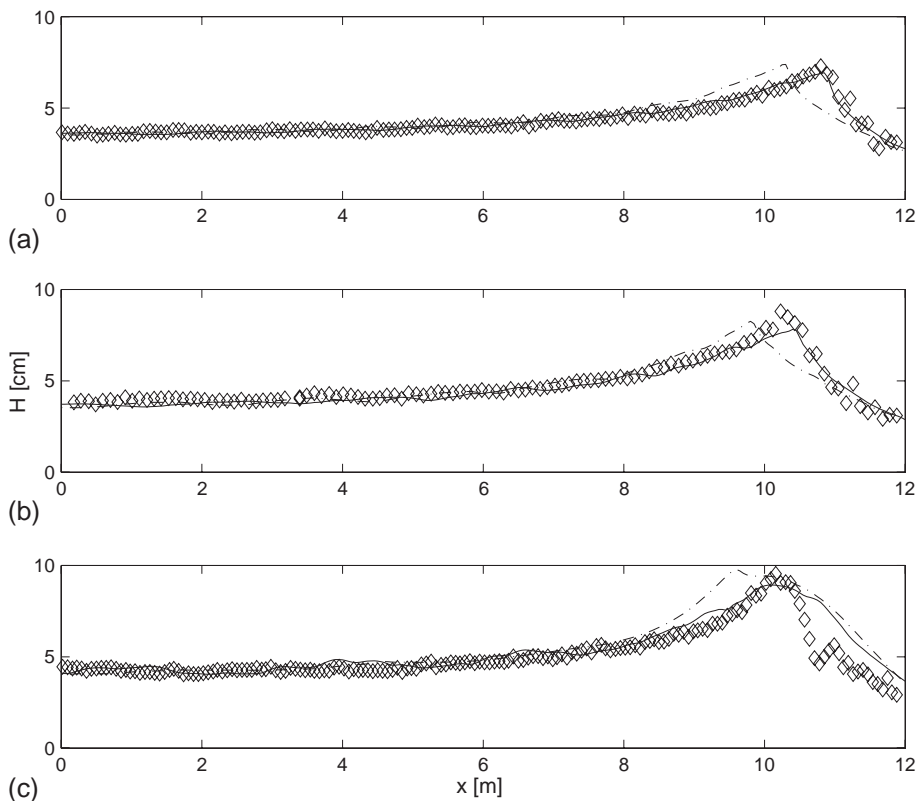


Fig. 6. Wave height distribution of regular waves on a plane beach. Solid line: fully nonlinear model; dash-dotted line: weakly nonlinear model (Veeramony and Svendsen, 2000); diamonds: data from Hansen and Svendsen (1979), $h_0=0.36m$, (a) Test O: $T=2.0s$, $H_0=0.038m$; (b) Test Q: $T=2.5s$, $H_0=0.040m$; (c) Test R: $T=3.33s$, $H_0=0.043m$.

Boussinesq model should be able to handle such a case, since equations that describe the surface position by just a vertical elevation at each horizontal point cannot describe the overturning or the double connected free surface flows, that occur during the first stages of a plunging breaker. The results shown in Fig. 6c show the difficulty the model has in representing such conditions. In particular within the transition region, the dissipation is not strong enough, while within the inner surf zone the agreement tends to be more acceptable and the overall model prediction, even if not very accurate, is quite reasonable in this case as well.

Within the shoaling region, Hansen and Svendsen (1979) provided the instantaneous time series for the surface profile at four locations (see Fig. 7), the last one being as close as possible to the breaking point (Fig. 7d). We see that the model agreement with experimental data is quite good for all the gage locations during shoaling, particularly for the fully nonlinear model, while the weakly nonlinear version shows again an overshoot, which leads to an early breaking (Fig. 7d). Again at the breaking point the wave height is slightly underpredicted by the fully nonlinear model. This behavior becomes more evident

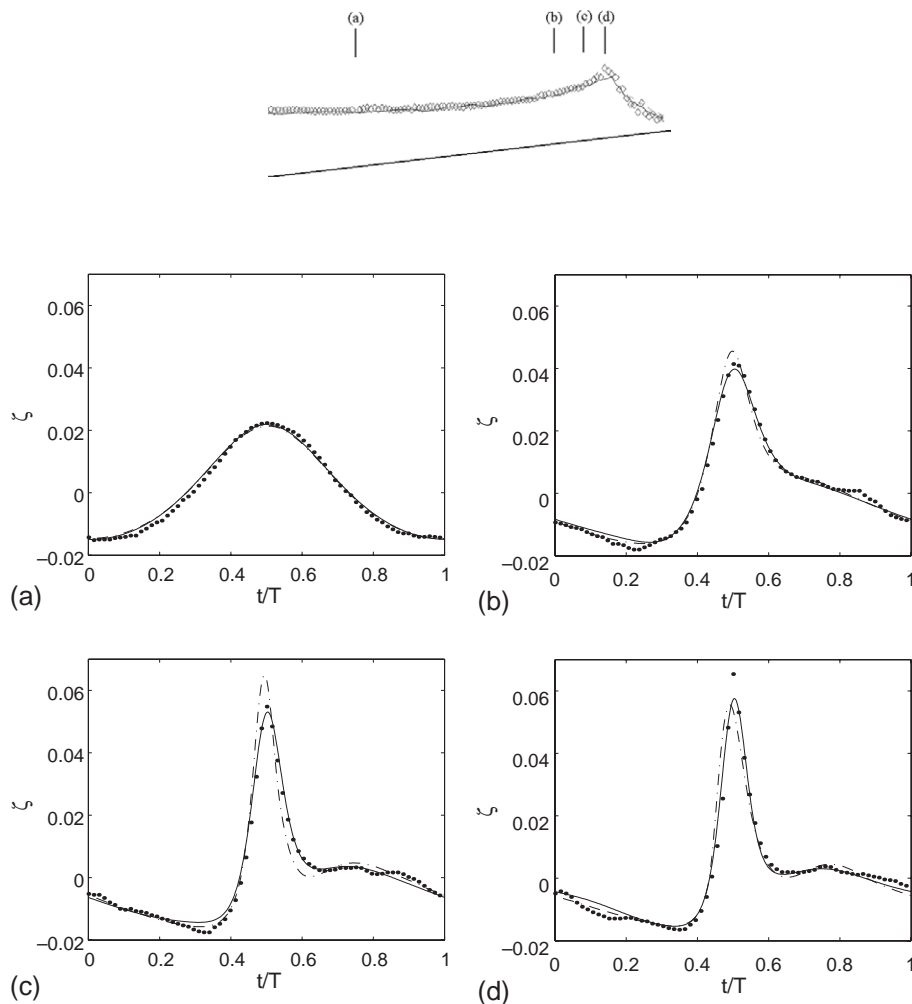


Fig. 7. Time series of the surface profile of a regular wave at different locations up to breaking. Solid line: fully nonlinear model; dash-dot line: weakly nonlinear model (V&2000); dots: data from Hansen and Svendsen (1979). $T=2.5s$, $H_0=0.040m$ at (a) $h/h_0=1.00$; (b) $h/h_0=0.38$; (c) $h/h_0=0.29$; (d) $h/h_0=0.27$.

with longer waves. Another apparent feature, shown in Fig. 7d, is that the experimental data show a secondary oscillation of the wave profile, which is recovered also by the Boussinesq model.

This analysis also confirms the good dispersive and nonlinear properties of the model. It is interesting to note that the choice of the depth integrated velocity \bar{u} as dependent variable gives good results, at least in the nearshore region, even though more complex approaches, such as the choice of a velocity at some particular reference level (see for example Madsen and Schäffer, 1998 and more recently Kennedy et al., 2001), have been proposed in order to improve the dispersive and nonlinear properties of Boussinesq-type of equations.

With respect to the surface profile's development within the surf zone, the experiments of Ting and Kirby (1996) have been considered for comparisons. The measurements were obtained on a plane beach with a slope very similar to that of Hansen and Svendsen (1979). Fig. 8 shows the comparisons of the surface profile evolution at four locations within the surf

zone. Ting and Kirby (1996) noted that the wave shape remains unchanged within the inner surf zone, which starts at $(x-x_b)/h_b=7.462$, where x_b and h_b are the location and the water depth at the breaking point respectively. The present fully nonlinear numerical model seems to reproduce the constant shape behavior quite well. However it can be observed both a slight overestimate of the crest elevation and the presence of a second harmonic of the surface profile, which is characteristic of Boussinesq-type models and which prevents the model itself from reproducing the well known saw-tooth shape. On the other hand the strong mismatch of the weakly nonlinear model results with the experimental data here is due to the poor representation of the shoaling properties, which in turn leads to an early breaking.

The model performance has also been compared to the data by Cox et al. (1995) which provides not only the surface profiles but also the velocity profiles for both nonbreaking and breaking waves. Cox et al. (1995) carried out their experiments using the same set-up of Ting and Kirby (1996). However, while the

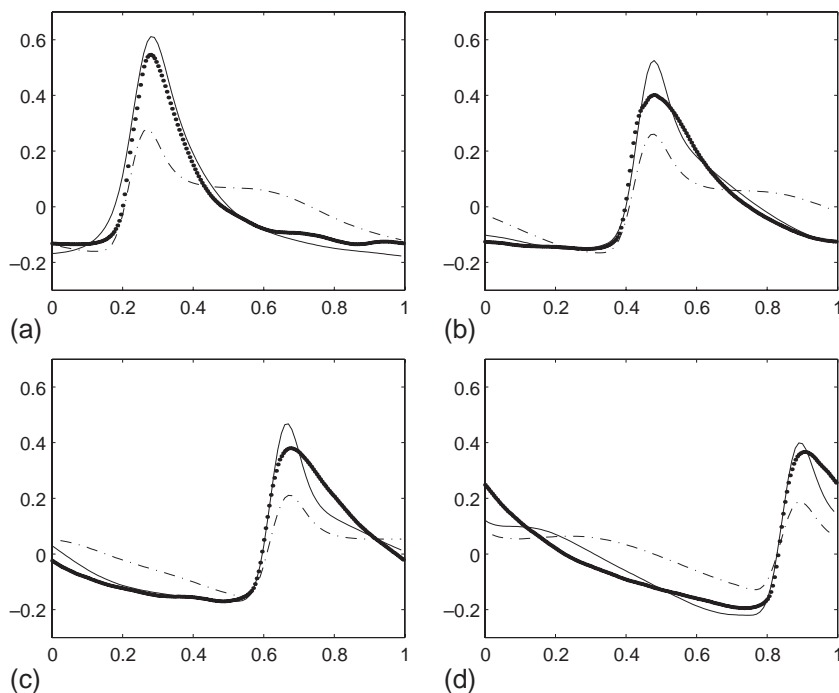
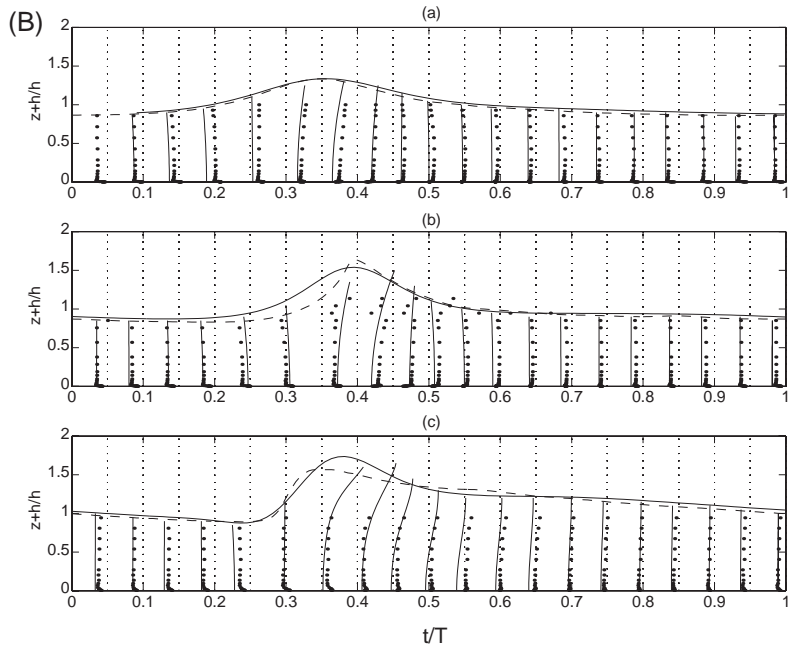
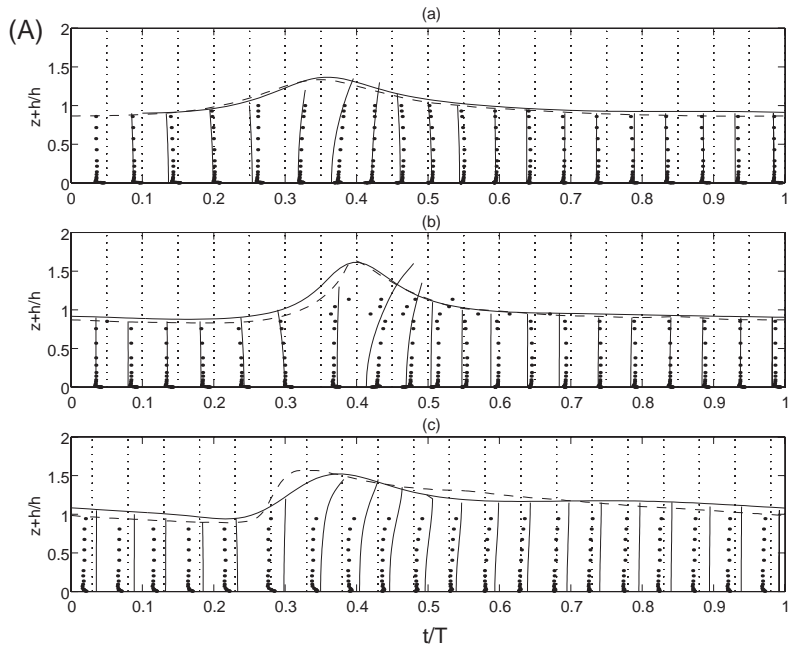
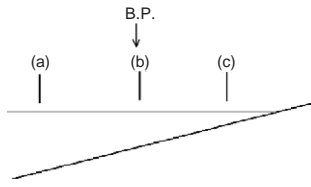


Fig. 8. Evolution of the surface profile of a regular breaking wave. Solid line: fully nonlinear model (V&2000); dash-dot line: weakly nonlinear model (V&2000); dots: data: from Ting and Kirby (1996). $T=2.0s$, $H_0=0.125m$ at (a) $(x-x_b)/h_b=4.397$; (b) $(x-x_b)/h_b=7.462$; (c) $(x-x_b)/h_b=10.528$; (d) $(x-x_b)/h_b=13.618$.



latter experiments had a smooth bottom, in the case of Cox et al. (1995) the bottom was made rough by gluing sand to it. It should be pointed out that in the present version neither Veeramony and Svendsen (2000) nor the present model account for dissipations due to the bottom boundary layer. Moreover the data of Cox et al. (1995) are phase-averaged, therefore the profiles appear smoother than those of Hansen and Svendsen (1979).

In Fig. 9 both the results from Veeramony and Svendsen (2000) and the present fully nonlinear model are reported along with the experimental data. Within the shoaling region (see Fig. 9Aa and Ba) the weakly nonlinear model and the present model provide basically the same results, as the velocity profile is almost constant. When the wave is about to break (see Fig. 9Ab and Bb), the data show a rate of shoaling which is in better agreement with Veeramony and Svendsen (2000)'s results. The velocity profiles predicted by the present fully nonlinear model, however, agree better with the data, while Veeramony and Svendsen (2000) underestimates the velocity under the crest.

Finally, within the surf zone (see Fig. 9Ac and Bc), it can be noticed that the agreement with the velocity data is again better for the present model. For the surface profile, it is found that the crest elevation is slightly overestimated. This is probably due to the nonlinear properties of the model. Indeed, the wave shape calculated with the present fully nonlinear model is closer to the measured one, particularly at the wave front. Moreover concerning the velocity profile, the overestimation of the velocity has essentially been eliminated.

In order to test the dispersive capabilities of the model, the wave celerity prediction has been tested in Fig. 10 against the experimental data of Hansen and Svendsen (1979).

The wave speed c is not an output of the numerical model, but can be estimated from the knowledge of the surface elevation. Indeed, generally speaking the wave speed c is expressed with reference to a well defined point of the surface profile. Here, after subtracting the mean water level from the time series

of the surface elevation, the zero-up crossing point of the surface profile has been chosen as representative one. Therefore c has been evaluated by moving averaging the celerity c_{inst} of each individual zero-up crossing point, which is expressed as

$$c_{\text{inst}} = \frac{\Delta x}{\Delta t_{\text{zero-up}}} \quad (81)$$

where Δx is the distance between two sections of the numerical grid and $\Delta t_{\text{zero-up}}$ is the time for the zero-up crossing point to go from the previous to the next section.

The numerical results match the data for the spilling breaker case (see panel (a) and (b)). It is noticed that for the case of a plunging breaker (Fig. 10c) the data show a quite big scatter at sections further offshore, probably due to the difficulty, also indicated by Hansen and Svendsen (1979), in detecting the reference point when small irregularities of the surface profiles are present. The present model seems to have the same problem for such a case.

Finally in Fig. 11 a comparison with the undertow profile measurements provided by Cox and Kobayashi (1997) is shown. It is pointed out that only a model accounting for the strong depth variation of the instantaneous velocity profile due to the rotational part of the velocity such as the one presented here is able to describe the vertical variation of the undertow current generated by the breaking waves. Irrotational Boussinesq models predict a depth uniform undertow profile, as is also demonstrated by the undertow profiles outside the breaking point. The agreement with data is quite good, except at the third section (Fig. 11c), where the wave has just started to break, and the simulated waves will start breaking a bit later. It may be worth reminding here that both models did not consider the effects of the bottom boundary layer, thus a finite velocity value is obtained at the bottom. In particular it can be noticed that the weakly nonlinear model of Veeramony and Svendsen (2000) overestimates both the undertow values at the bottom and the slope of the undertow profile, while the fully nonlinear model proposed here is able to better reproduce the real dynamics of such a phenomenon.

Fig. 9. Comparisons on velocity profiles at different locations as measured by Cox et al. (1995) (dots) with (A) weakly nonlinear model of Veeramony and Svendsen (2000); (B) fully nonlinear model. $H=0.115\text{m}$, $T=2.2\text{s}$, (a) $h/h_0=0.70$ (shoaling zone); (b) $h/h_0=0.53$ (close to the breaking point); (c) $h/h_0=0.27$ (inner surf zone).

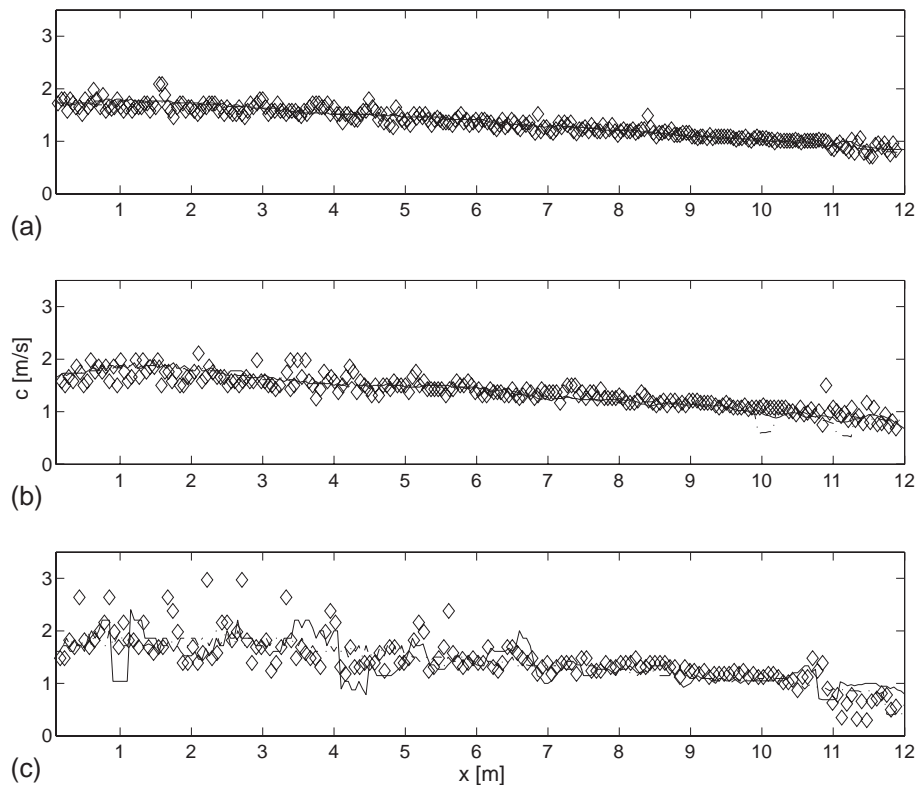


Fig. 10. Wave speed distribution as obtained propagating regular waves on a plane beach. Solid line: fully nonlinear model; dash-dotted line: weakly nonlinear model of Veeramony and Svendsen (2000); diamonds: data from Hansen and Svendsen (1979). (a) Test O: $T=2.0s$, $H_0=0.038m$; (b) Test Q: $T=2.5s$, $H_0=0.040m$; (c) Test R: $T=3.33s$, $H_0=0.043m$, $h_0=0.36 m$.

Such a characteristic, in particular, is extremely important for the prediction of the net sediment transport in nearshore regions.

4.2. Wave groups

Comparisons of the proposed model with the experimental data of Svendsen and Veeramony (2001) are also presented. Particularly the time series of the free surface and the spatial distribution of the wave heights, both outside and inside the surf zone, are analyzed.

It may be worth noticing that instead of adding together two sinusoidal waves with slightly different frequencies, the wave groups in Svendsen and Veeramony (2001) were generated at the wavemaker by patching together five cnoidal waves with the same wave period but different wave heights.

A preliminary analysis of the raw experimental data was carried out in order to specify the input

wave group for the model. The specific aim of the present work is to analyze the short wave motion. However, the irregular characteristics of the waves, cause also generation of a long-wave motion in the laboratory tank as well as inside our computational domain. The main difference between the laboratory and the numerical wave tank was that the first one had a moving shoreline, whereas in the latter a sponge layer along with a wall boundary condition at the end of the tank were used. Preliminary analysis have shown that the simulation of the correct long wave effect would require a different shoreline boundary condition, so such a phenomenon is not covered in the present paper. Therefore, a high pass filter has been used to cut off frequencies much lower than the peak frequency f_p . This also implies that we are not in these computations including any possible influence such low frequency oscillations might have on the breaking characteristics.

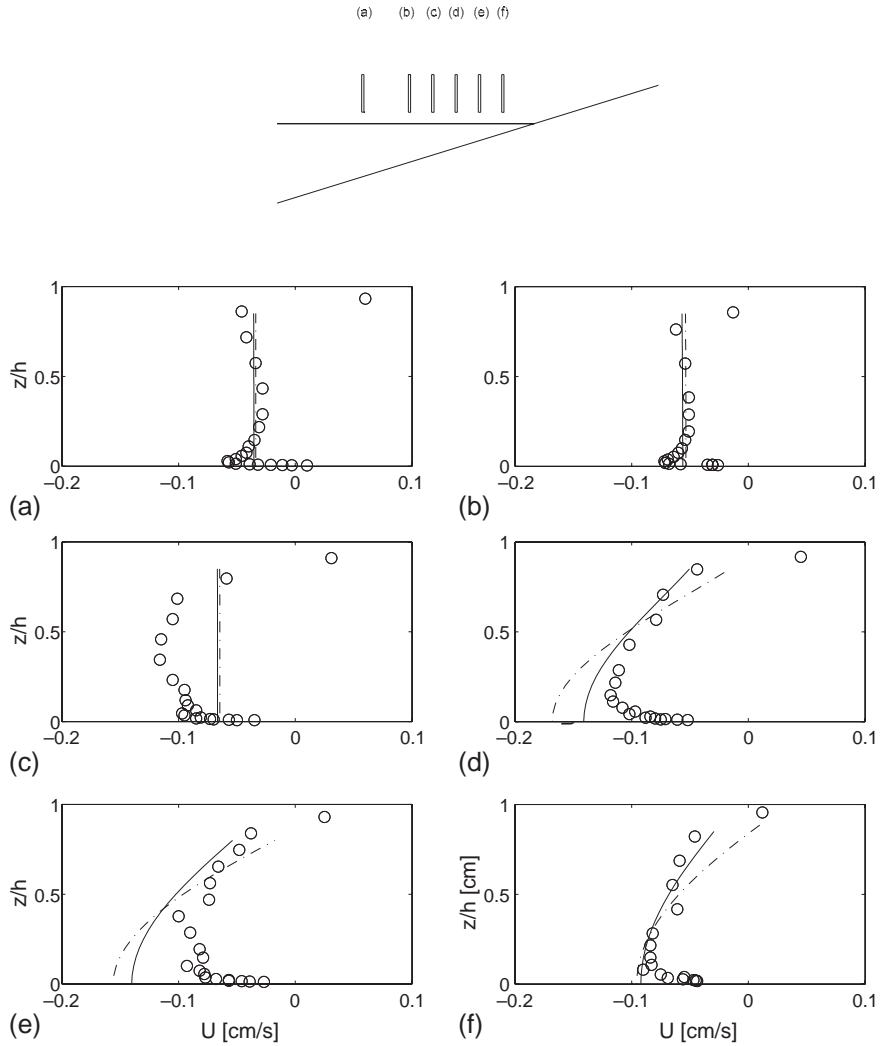


Fig. 11. Undertow of regular waves propagating on a plane beach at different locations. Solid line: fully nonlinear model; dash-dotted line: weakly nonlinear model; circles: data from Cox and Kobayashi (1997). $H=0.115m$, $T=2.2s$. (a) $h/h_0=0.70$; (b) $h/h_0=0.53$ (shoaling zone); (c) $h/h_0=0.44$ (transition region); (d) $h/h_0=0.36$; (e) $h/h_0=0.27$; (f) $h/h_0=0.18$ (inner surf zone).

As waves propagating over the slope have different wave heights, the shoaling process will increase the wave heights differently. At the same time an energy exchange between different frequencies takes place. Therefore each individual wave of the group reaches the breaking condition at a different location. Therefore how and where the single wave starts to break is difficult to predict and at the same time is extremely important for the pattern of the free surface variation inside the breaking zone.

Svendsen and Veeramony (2001) measured the time variation of the breaking point location, providing then the opportunity to verify the behavior of the model with respect to such an important mechanism. In Fig. 12, the results obtained for two different case studies, characterized by different values of the wave groupiness ($G=\pm 20$ and $G=\pm 50$, respectively) are compared with the experimental data. The results from the model are averaged over about 10 group periods. As the wave groupiness increases, the breaking zone, i.e. the

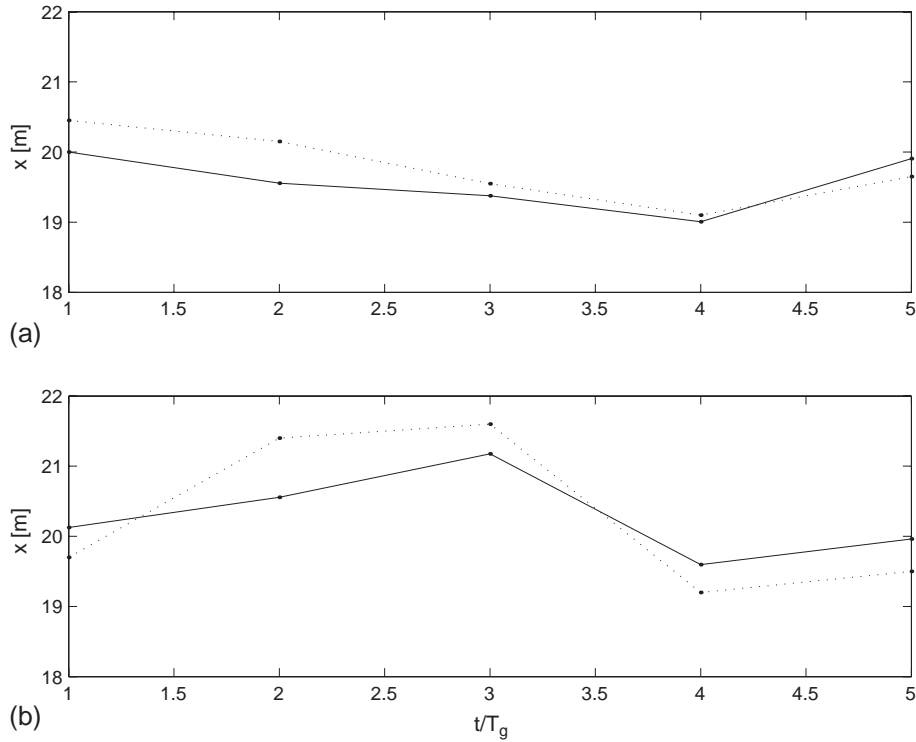


Fig. 12. Time variation of the breaking point position along the tank. (a) Test W03, $H_m/h_0=0.237$; $G=\pm 20\%$; (b) Test W06, $H_m/h_0=0.25$; $G=\pm 50\%$. (dashed line: data from Svendsen and Veeratomy (2001); solid line: fully nonlinear model results).

region where the waves start breaking, becomes larger. The model is able to catch properly this spatial and time variation of the moving breaking point, even though it underpredicts the width of the breaking zone in the case with 50% groupiness.

Fig. 13 shows the comparisons with the measured surface elevation time series. The first two panels correspond to sections in the shoaling zone, while the last three are inside the surf zone. The agreement of the calculated free surface is fairly good, in both regions. In particular it can be noticed that both in the experimental measurements and in the numerical data the groupiness of the waves is conserved after the breaking point.

It should also be noticed that at some stage there is a phase shift of the smallest waves within the group with respect to the data. As an example, see Fig. 13c where the four waves after the highest wave are all out of phase with respect to data, and Fig. 13d, where the first two of these waves are again in phase with the measured ones. Such a behavior could be due to

the different long wave motion within the physical and the numerical tank.

In order to illustrate such a discrepancy, an analysis of the time variation of the mean water level has been carried out, by averaging the surface elevation within each wave group according to the following expression

$$\text{MWL}_g = \frac{1}{5T_g} \int_{t_i}^{t_i+5T_g} \eta \, dt \quad \text{for } t_i = 0, 5T_g, 10T_g, \dots \quad (82)$$

where T_g is the period of each wave within the group. The time variation of the mean water level MWL_g calculated by the model is plotted in Fig. 14 against those obtained with an analogous analysis of the raw experimental data. The comparison between the computed and the measured MWL_g shows a fairly good agreement in the deeper part of the domain, up to $h/h_0=0.287$, whereas the mean water level is overestimated in shallower waters. Moreover

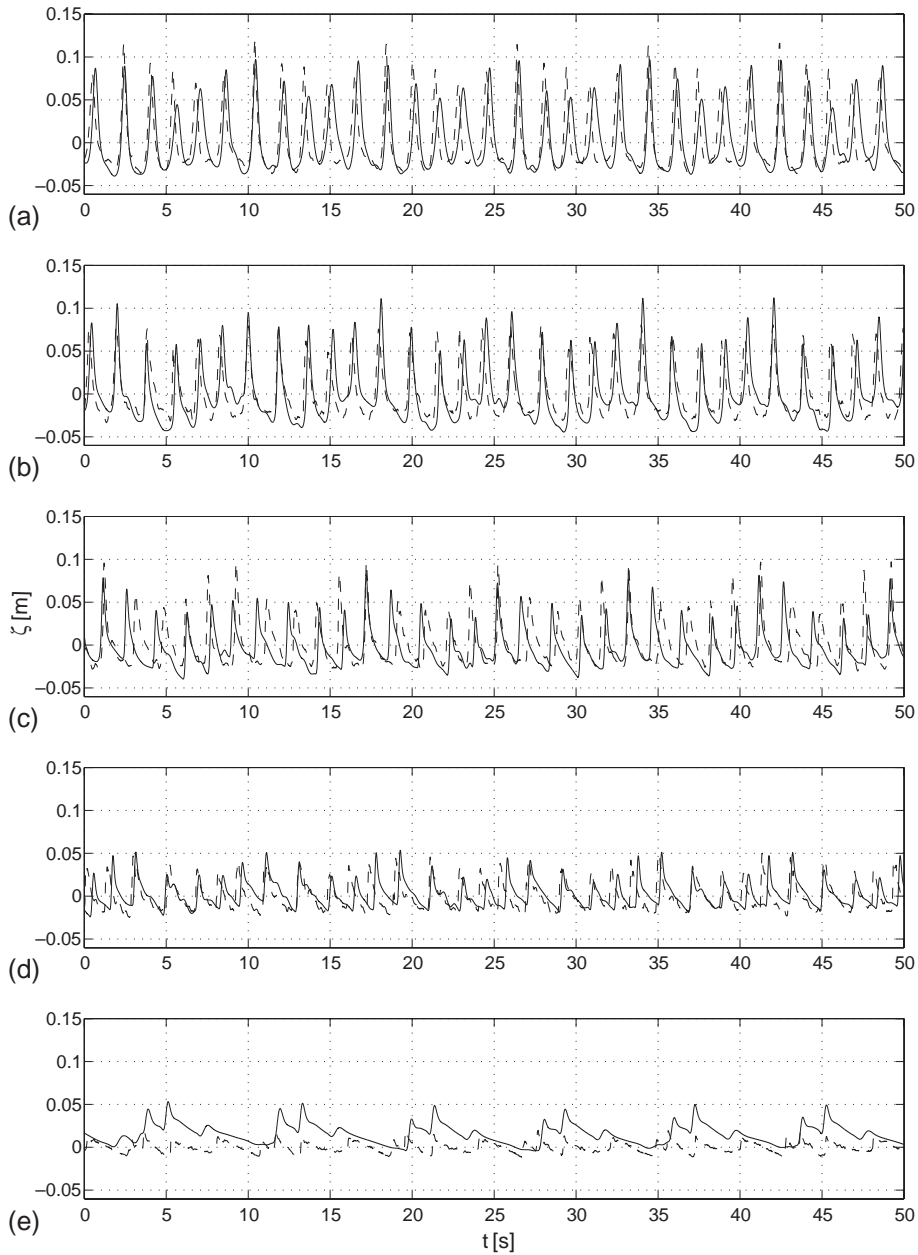


Fig. 13. Time series of the surface elevation for group waves at different locations. Solid line: fully nonlinear model results; dashed line: data from Svendsen and Veeramony (2001), Test W06, $H_m/h_0=0.25$, $G=\pm 50\%$. (a) $h/h_0=0.525$; (b) $h/h_0=0.382$; (c) $h/h_0=0.311$; (d) $h/h_0=0.239$; (e) $h/h_0=0.054$.

it should be noticed that in the simulations long-period oscillations appear, whereas the experimental data do not show any of such strong variations. Those long oscillations could influence the perio-

dicity of the calculated surface profile and thus they could be responsible for the aforementioned phase differences between the computed and the measured surface profile.

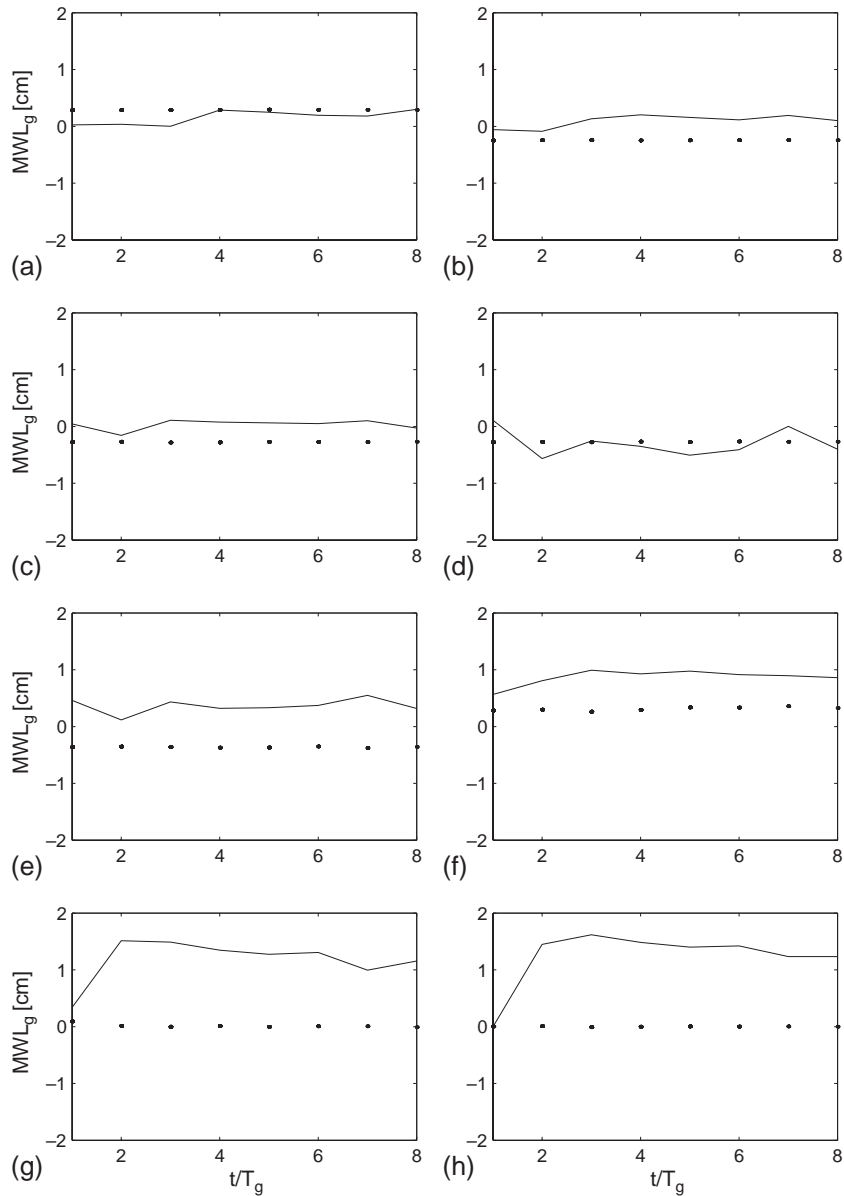


Fig. 14. Time variation of the mean water level within every single group, MWL_g , at several sections along the tank for the condition of Test W03, $H_m/h_0=0.237$, $G=\pm 20\%$. Solid line: fully nonlinear model results; dots: experimental data from Svendsen and Veeramony (2001). (a) $h/h_0=1.000$; (b) $h/h_0=0.587$; (c) $h/h_0=0.454$; (d) $h/h_0=0.394$; (e) $h/h_0=0.343$; (f) $h/h_0=0.287$; (g) $h/h_0=0.236$; (h) $h/h_0=0.184$.

Moreover, Svendsen and Veeramony (2001) noticed in their data a change of the position of the highest waves of the group, relative to the others. They noticed also that both before breaking and close to the shoreline some of the individual waves of the group increase their period (and thus their length) at

the expense of other waves of the same group, due to the fact that the highest waves travel faster than the smallest ones. These variations occurs within the wave group, since obviously the group period cannot change. This process is more evident when the groupiness is higher. As Fig. 15 shows the model

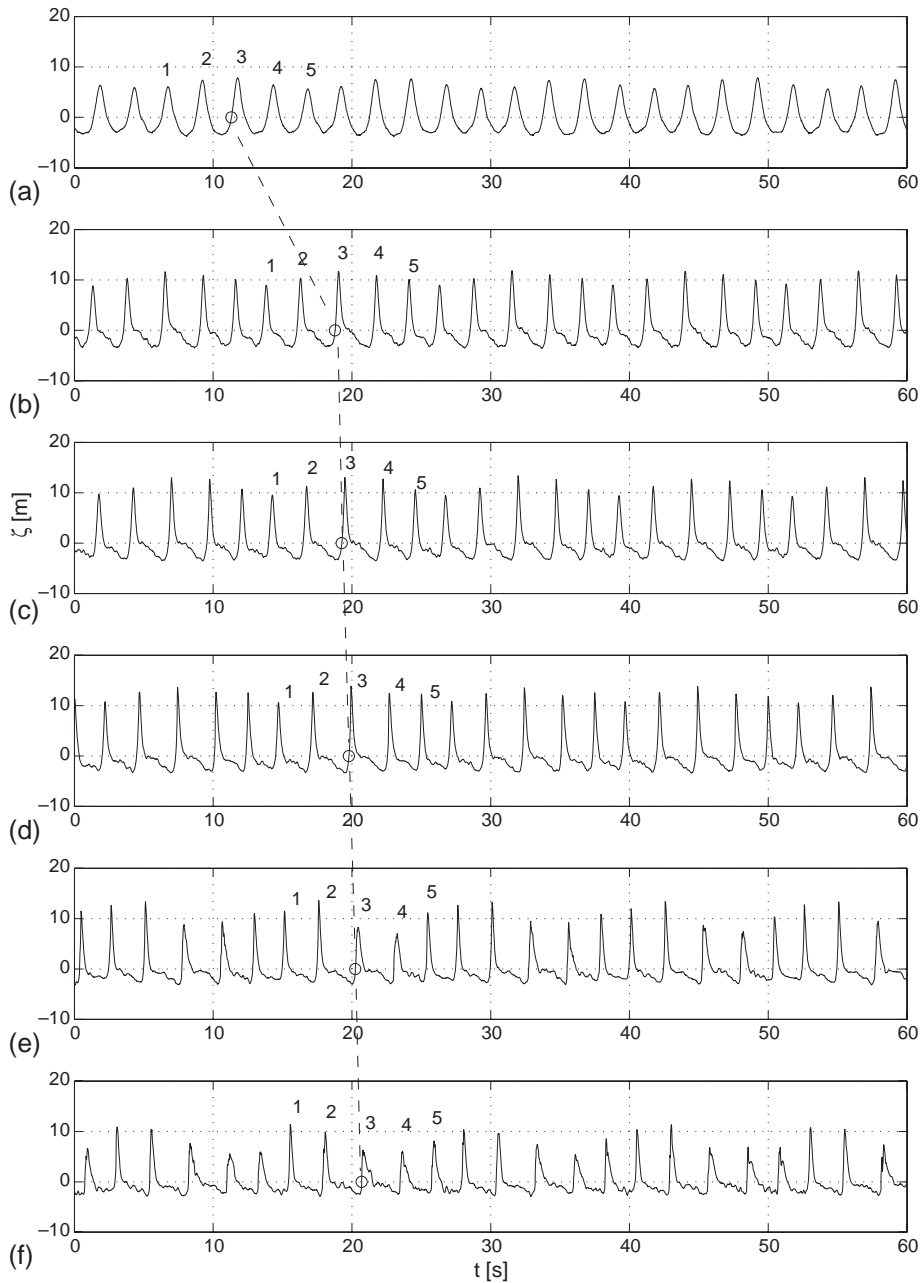


Fig. 15. Time evolution of a single wave group (waves: 1, 2, 3, 4, 5) which propagates over a plane beach as calculated by the fully nonlinear model. (a) $h/h_0=0.554$; (b) $h/h_0=0.504$; (c) $h/h_0=0.454$; (d) $h/h_0=0.404$; (e) $h/h_0=0.354$; (f) $h/h_0=0.303$.

recovers pretty well the aforementioned features, such as the changes of wave height distribution inside the group and the period and length variation of the individual waves.

The spectral characteristics of the computed surface profile have been compared with those of the measured one. In Fig. 16 the power spectra are reported at different sections along the slope, starting

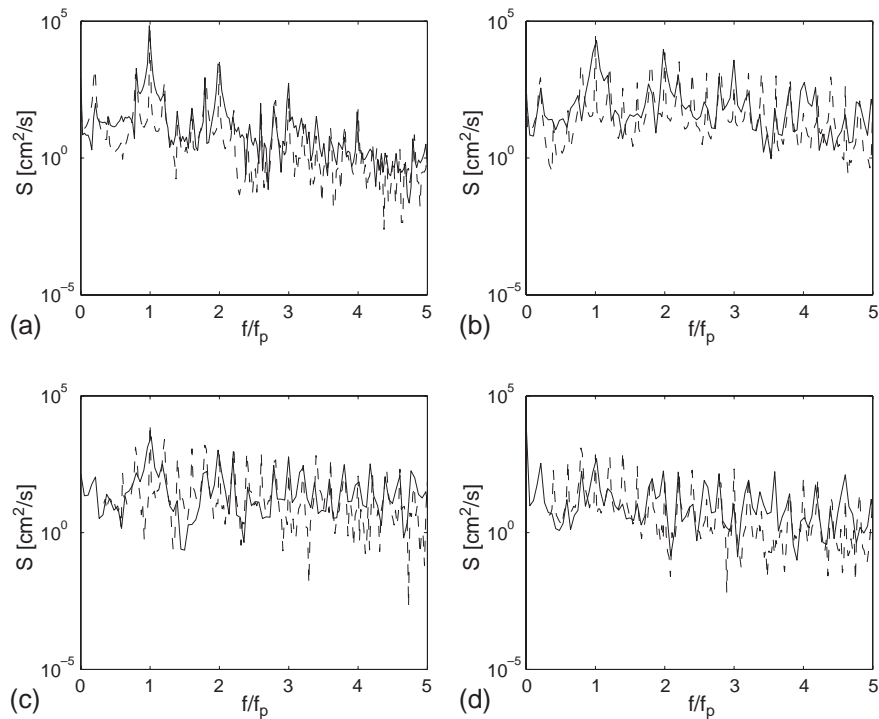


Fig. 16. Power spectrum of the surface profile for case W03, $H_m/h_0=0.237$, $G=\pm 20\%$ at (a) $h/h_0=1.000$; (b) $h/h_0=0.539$; (c) $h/h_0=0.325$; (d) $h/h_0=0.1465$. Solid line: fully nonlinear model results; dashed line: experimental data from Svendsen and Veeramony (2001).

from the toe of the shore (see Fig. 16a). It can be noticed that both in the measurements and in the numerical results at the beginning of the slope the main energy content is concentrated at the peak frequency and at its harmonics. On the other hand, the model results, as well as the measurements, also show that energy of the long waves is at the groupiness period $f_p/5$. As the waves move shoreward the power spectrum of the experimental data show additional peaks at multiples of the group period, which are due to nonlinear interactions. While the trend of the computed power spectrum agrees fairly well with the data, the model transfer of energy at the neighboring frequency appears sometimes weaker with respect to the data.

Since the wave groups at the offshore boundary were generated as in the experiments, i.e. patching together five different cnoidal waves with different wave heights having the same wave period, here for each component of the wave group the spatial distribution of wave height along the x -axis is shown in Fig. 17 and compared with the experimental data.

The wave heights have been recovered from the time series of the surface profiles by analyzing the history of the waves, that is by following the waves as they move forward, as schematically shown by Fig. 15, where the propagation of Wave 3 is followed both in time and space.

Fig. 17 shows the comparisons with data distinguishing between Wave 1, Wave 2, Wave 3, Wave 4 and Wave 5, respectively. The agreement is very good both in the shoaling region and in the inner surf zone. The very satisfactory wave height prediction within such a large surf zone is worth to notice, because it confirms the good dissipation properties of the model, which is entirely due to the effects of the roller. In the transition region, particularly for Wave 1 and Wave 2, which are also the smallest waves of the group (see Fig. 17a and b), the experimental data show a double trend, one with a positive curvature of the distribution, i.e. with a trend more similar to that of the other components and similar to the model results, the other with a negative curvature which the model is not able to reproduce. The first type of behavior is physically

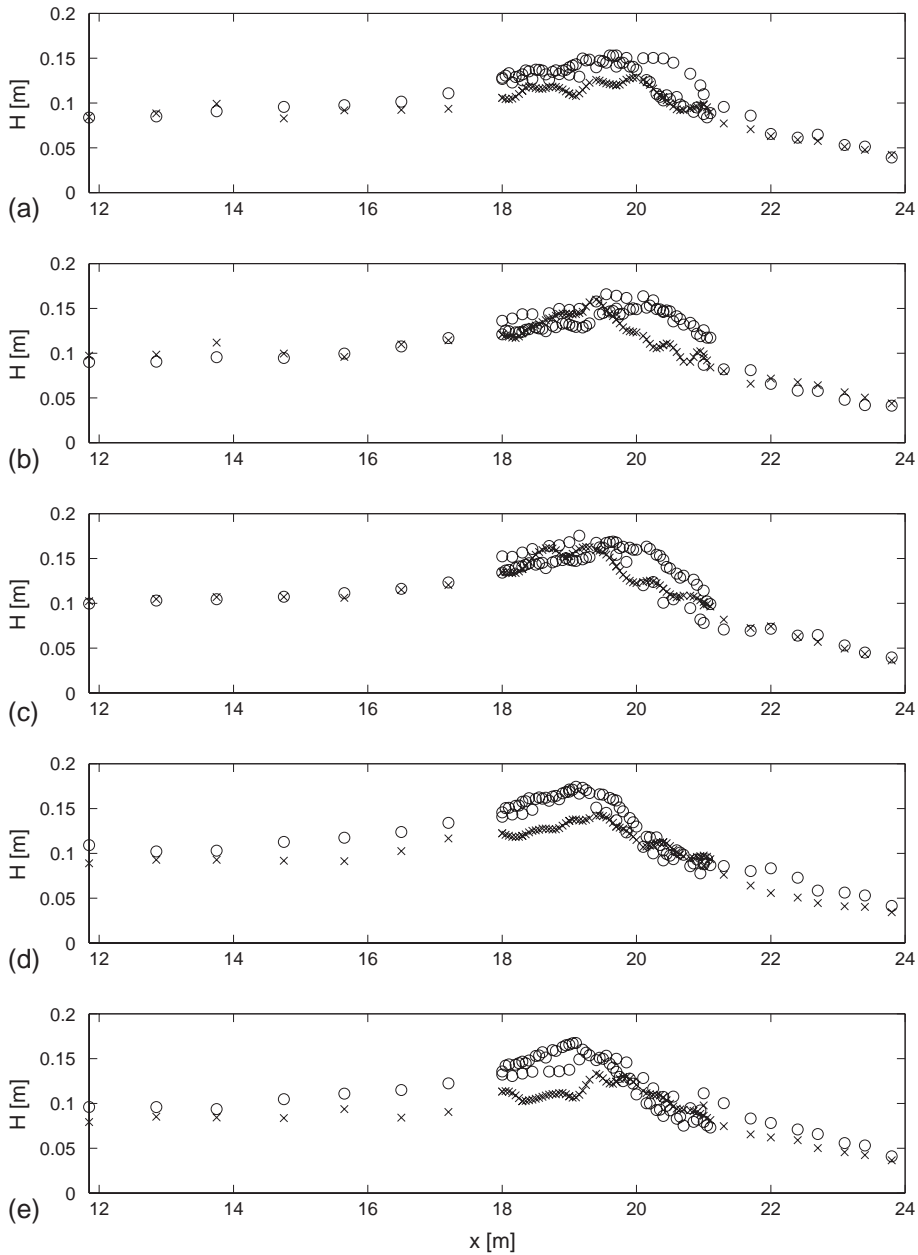


Fig. 17. Wave height distributions along the plane beach. (Circles: fully nonlinear model results; crosses: data from Svendsen and Veeramony (2001), case W03, $H_m/h_0=0.237$, $G=\pm 20\%$, with reference to Fig. 15(a) Wave 1; (b) Wave 2; (c) Wave 3; (d) Wave 4, (e) Wave 5).

associated with a well defined position of the breaking point and to smoother changes of the wave characteristics at the first instant of breaking, while the other type could be due to an unstable equilibrium of wave configuration, such as the breaking can occur sooner

or later on the slope. When this latter condition occurs, i. e. when after some instability the wave starts breaking more onshore, the energy dissipation gradient has to be larger, as the total energy to be dissipated is always the same, no matter where the

breaking point is located. Indeed the wave height experimental data in Fig. 17a and b show an higher gradient for the second trend right after breaking. Then at some point within the inner surf zone the two conditions get to the same value of wave height (see Fig. 17a) and from there on show the same trend again.

5. Model characteristics at breaking

As the model aims at improving the description of waves propagating within the surf zone, some peculiar features of the model related to the breaking have been analyzed.

5.1. Breaking criterion

The main limitation of the Boussinesq models is probably due to their inability to intrinsically predict where and when the breaking starts. Indeed an external, empirically calibrated criterion is necessary in order to trigger the breaking. Here the one proposed by Schäffer et al. (1993), based on a critical value of the wave steepness, has been adopted, since it allowed for easily determining the roller location.

In particular, such a criterion set the initiation of breaking when the slope of the waves reaches the critical value α_b , which in the present model has been assumed equal to 30, while the breaking is stopped if the wave slope is less than α_0 , here equal to 10. It should be pointed out that the first value, which is higher than the range suggested by Schäffer et al. (1993), allows for simulating better the position of the breaking point.

In order to show an interesting extra feature of the present model, the adopted criterion has been tested against the Stokes criterion, based on the surface velocity, which in contrast to many other criteria does not need any calibration procedure.

Indeed, for a breaking wave: the surface particles, located downstream with respect to the crest (point 3 in Fig. 18a), are accelerated downward and move faster than the wave, then a turbulent shear is generated to sustain this motion; the surface particles upstream (point 1 in Fig. 18a) move with a velocity smaller than the wave speed c , since there is no force able to accelerate them upward, while at the crest

(point 2 in Fig. 18a) the surface velocity is about equal to c . Thus, in other words, the continuous steepening of the front, due to the vertical acceleration, is limited by the generation of shear stresses, which reach their maximum value close to the lower edge of the roller. Therefore a very delicate test for the model prediction capabilities is the evaluation of u_s compared to c . As a confirmation of the quite good breaking prediction, Fig. 18b shows the ratio u_s/c for a breaking wave (as a reference the dimensionless surface profile ζ/h has also been shown). It may be noticed that the ratio u_s/c is always less than one on the back of the wave and that the maximum of velocity occurs close to the crest on the wave front.

It is worth pointing out that an important feature of the criterion based on the surface velocity and the wave speed is that there are no empirical parameters to be calibrated. Thus, from a physical point of view, it is remarkable that the model results agree, at least qualitatively, in a fairly good manner with such a criterion, even though the philosophy of the breaking criterion implemented into the model is quite different from that of the Stokes breaking criterion.

5.2. Vorticity dynamics

As already stressed, the main novelty of the model of Veeramony and Svendsen (2000), improved in the one presented here, is that the distribution of vorticity due to wave breaking is included as an essential part of the flow inside the surf zone. As a matter of fact, the presence of vorticity inside the flow allows us to derive the expressions for the breaking terms, which represents the excess of momentum flux relative to an irrotational Boussinesq model. This is also the contribution to the momentum flux that causes the energy dissipation due to the breaking process.

Fig. 19 shows the time variation of the vorticity during the breaking processes at three sections, the first one being very close to the breaking point, where breaking starts, the second one in the transition region and the third one within the inner surf zone. The vorticity, generated at the lower edge of the roller region, is both spread downwards by diffusion mechanisms and is left behind as the wave propagates onwards. As a dual to the aforementioned mechanism, Fig. 20 shows the evolutions of the corresponding

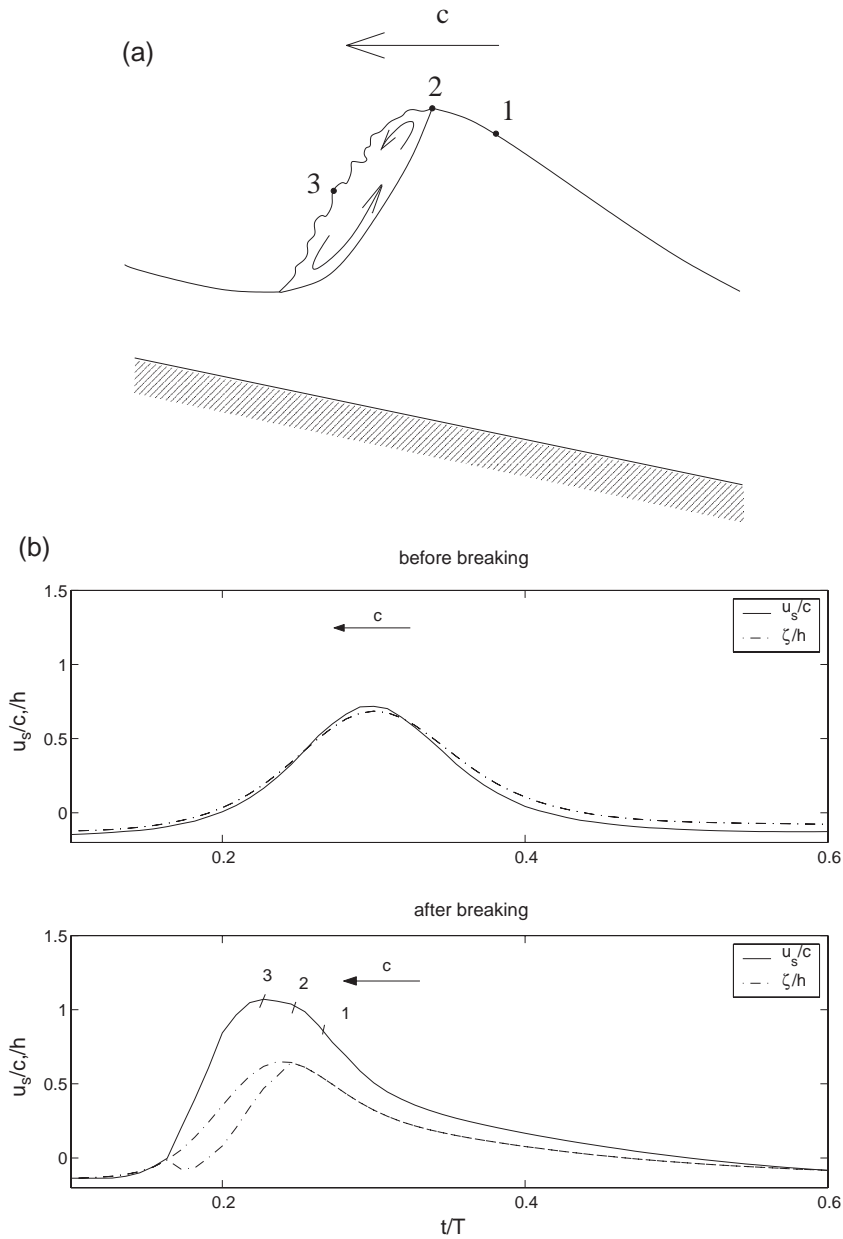


Fig. 18. Ex-post validation of the adopted breaking criterion: (a) sketch of Stokes breaking criterion; (b) model results on both the surface velocity (solid line: u_s/c) and surface elevation (dashed dot line: ζ/h) time series of a breaking wave.

breaking terms. It appears that the contribution to the pressure $(\Delta P)_{xx}$ due to the action of the roller plays the key role during the first stages of breaking but it decays as the wave moves onshore, while the excess of momentum flux due to the vertical distribution of

the vorticity, $(\Delta M)_x$, tends to eventually be the main responsible for dissipating wave energy as the propagation continues. Also contributions like the action exerted by the adjacent water columns, D_{uw} , cannot be neglected.

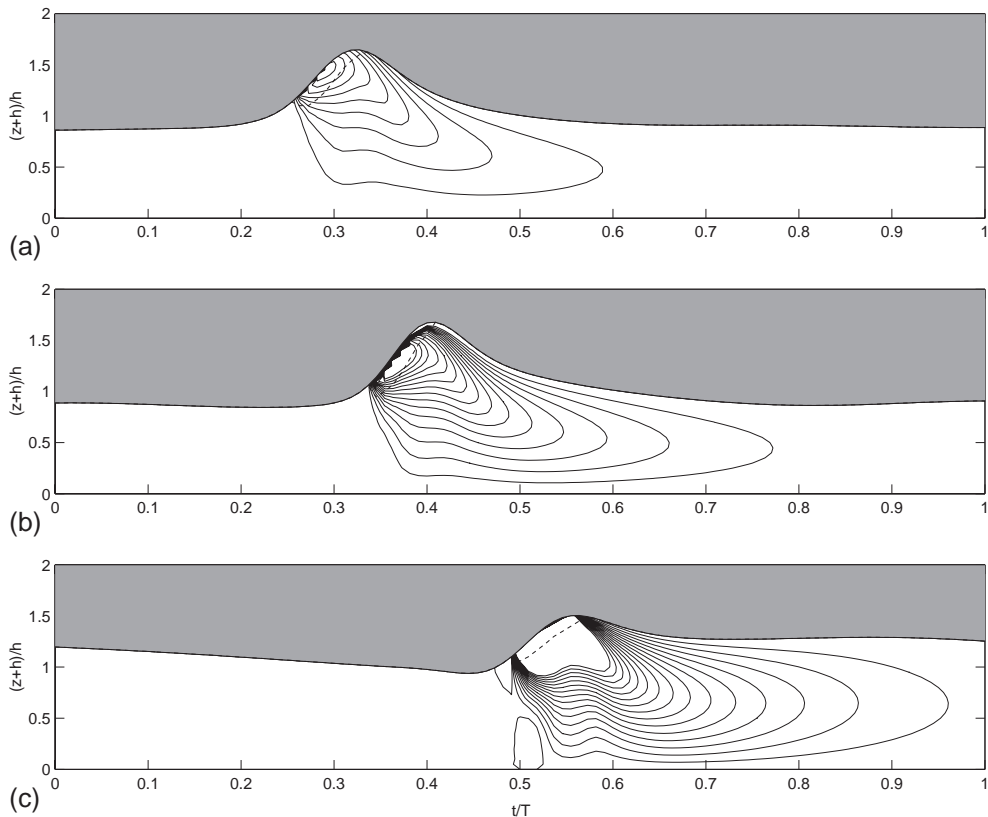


Fig. 19. Contour lines of the vorticity distribution under a breaking wave: (a) as the breaking starts; (b) within the transition region; (c) within the inner surf zone.

Considering the hydraulic similarity between breaking waves and hydraulic jumps, it can be noticed that the excess of momentum flux in breaking waves acts similarly to that generated in hydraulic jumps (Svendsen et al., 2000). Indeed, in both cases, it is necessary to satisfy the momentum balance and also to prevent the steepening of the turbulent front. Besides, considering the case of a hydraulic jump, the only significant breaking term is $(\Delta M)_x$, since the term $(\Delta P)_{xxt}$ vanishes for the steady-current case and all the other terms are quite small. Considering the analysis on weak turbulent hydraulic jumps carried out by Svendsen et al. (2000), other similarities between the two types of flow can be noticed. Indeed, in both cases the maximum of the excess of momentum flux appears within the roller region, close to the toe and it does not die out, but it remains quite large much further

downstream of the end of the actual roller (see Fig. 20 here and Fig. 6 in Svendsen et al., 2000).

6. Conclusions

A fully nonlinear Boussinesq model for breaking waves has been derived and implemented by assuming that the motion of the breaking waves is rotational. The vorticity generated by the breaking has been determined by solution of the vorticity equation in addition to the Boussinesq equations for the full motion. Such a model can be seen as an extension of the weakly nonlinear one developed by Veeramony and Svendsen (2000).

In order to improve the modeling of the rapid variations in the motion in the neighborhood of the turbulent front of the breaking wave, a self-adaptive,

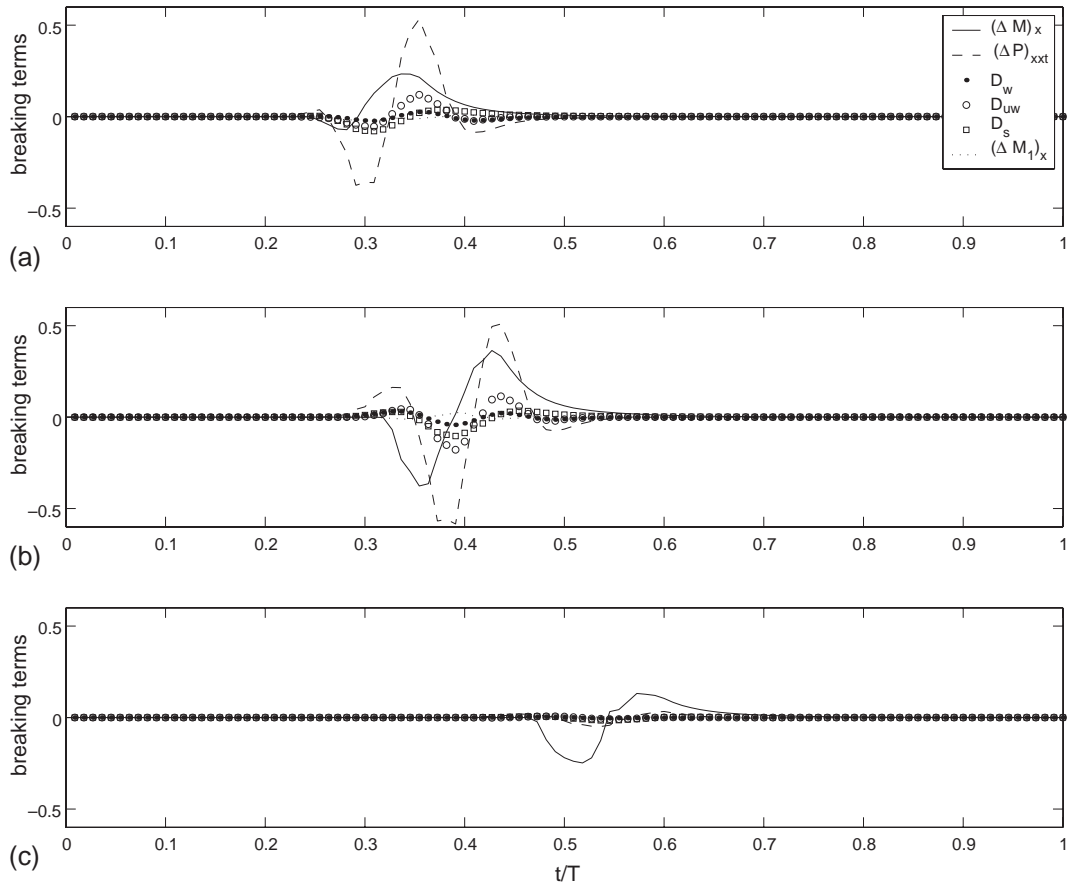


Fig. 20. Time series of the breaking terms of Eq. (23): (a) as the breaking starts; (b) within the transition region; (c) within the inner surf zone.

time-varying grid has been implemented in the roller region of the waves. This new algorithm allows to make the computational grid points move with the roller and moreover to refine the grid at the toe of the roller, where the most rapid variations occur in the relevant variables.

The validation of the model was organised in two stages. Initially, for the case of regular breaking waves, the results of the fully nonlinear model proposed here were compared both with the numerical results of the weakly nonlinear model of Veeramony and Svendsen (2000) and with literature experimental data. Then, the fully nonlinear version was tested against irregular waves (in the form of wave groups published by Svendsen and Veeramony, 2001). The latter data set included information about time and space varying breaking points similar to what occurs in random waves.

From the aforementioned analysis it turned out that:

- In the shoaling zone, before breaking, the proposed fully nonlinear model eliminates the overshooting due to the inaccuracy of the weakly nonlinear model of Veeramony and Svendsen (2000), which thus strongly affects the results within the surf zone.
- The good prediction of the wave height variation of the present model is very accurate both within the shoaling and the surf zone, showing that the breaking terms and the energy dissipation have been modeled appropriately. This was found true also for plunging breaker, where the numerical results were reasonable, even though, in principle, this kind of breakers cannot be handled by such a model.

- The comparisons with the very detailed data from Hansen and Svendsen (1979) showed that the model is able to predict quite accurately the flow conditions, both in the shoaling region and inside the surf zone, supporting also the choice of the depth averaged velocity as reference velocity for the Boussinesq model.
- The comparisons with the velocity field data of Cox et al. (1995) showed that the present model allows to correctly estimate the increase of velocity under the crest of a breaking wave, as opposite to the weakly nonlinear model, which overestimated it. Following the assumption of the roller effects, also comparison with undertow profiles were possible, showing that also in this case the present model provides quite better predictions than Veeramony and Svendsen (2000)'s model.
- The quite good comparisons with the measurements of wave height and surface profile in the case of groupy waves also demonstrated that the model is able to recover the moving breaking line, which is a characteristic of irregular waves, and the effects of the breaking process on the groupiness of the waves, such as the wave phase shift and the transfer of wave energy at multiples of the group frequency.

Finally, by analyzing some features of waves at breaking, an ex-post validation of the breaking criterion was performed, thus supporting at least qualitatively the realistic behavior of the model also from this critical point of view.

Acknowledgements

Prof. Enrico Foti of the University of Catania, Prof. Maurizio Brocchini of University of Genova and Riccardo Briganti of University of Roma3 are acknowledged for many helpful discussions. This work has been partly founded by the GNDCI of CNR (Project: “Estimation and reduction of the risk in the coastal area”), by the MIUR (Project: “Hydrodynamics and Morphodynamics of Tidal forced Environments”, the SandPit (Contract No. EVK3-CT-2001-00056) and by the Office of Naval Research/National Oceanographic Partnership Program (Award No. N00014-99-1-1051).

Appendix A. Calculation of breaking terms

The expression for the breaking terms can be derived from the value of the rotational velocity u_r , computed from the analytical solution of the vorticity transport equation, expressed as

$$\omega = \begin{cases} \sum_{n=1}^{\infty} G_n \sin n\pi\sigma & z < \zeta_e \\ \omega_s \left(\frac{\zeta - z}{\zeta - \zeta_e} \right) & \zeta_e < z < \zeta \end{cases} \quad (83)$$

The contribution from the roller region to the vorticity profile has been included by approximating the vorticity through a linear polynomial, which has the value of ω_s at the lower edge of the roller and zero at the surface. Therefore the expression of the rotational velocity reads

$$u_r = \begin{cases} \int_{-h}^z \omega \, dz & z < \zeta_e \\ u_{rb} + \int_{\zeta_e}^z \omega \, dz & \zeta_e < z < \zeta \end{cases} \quad (84)$$

with u_{rb} being the rotational velocity at the lower edge of the roller.

The expressions used for computing the breaking terms are reported in Eqs. (85) and (86), and are derived under the assumptions that for the $O(\mu^2)$ terms, namely ΔP_{xxt} , ΔM_1 , D_w and D_{uw} , the contribution coming from the roller region is assumed to be small.

$$\begin{aligned} \Delta M = (h + \zeta_e)^3 & \left[\left(\sum_{n=1}^{\infty} \frac{G_n}{n\pi} \right)^2 + \frac{1}{2} \sum_{n=1}^{\infty} \frac{G_n^2}{n^2 \pi^2} \right] \\ & + u_{rb}^2 (\zeta - \zeta_e) + \frac{2}{3} u_{rb} \omega_s (\zeta - \zeta_e)^2 + \frac{2}{15} \omega_s^2 (\zeta - \zeta_e)^3 \\ & - \frac{\left[(h + \zeta_e)^2 \sum_{n=1}^{\infty} \frac{G_n}{n\pi} + u_{rb} (\zeta - \zeta_e) + \frac{1}{3} \omega_s (\zeta - \zeta_e) \right]}{h + \zeta} \end{aligned} \quad (85)$$

$$\begin{aligned} (\Delta P)_{xxt} = \frac{\partial^2}{\partial x^2} & \left(- (h + \zeta_e)^4 \sum_{n=1}^{\infty} \frac{\partial G_n}{\partial t} \frac{(-1)^n}{n^3 \pi^3} \right. \\ & \left. - 4(h + \zeta_e)^3 \frac{\partial \zeta_e}{\partial t} \sum_{n=1}^{\infty} \frac{G_n (-1)^n}{n^3 \pi^3} \right) \end{aligned} \quad (86)$$

$$\Delta M_1 = 2\bar{u}_{pxx}(h + \zeta_e)^4 \sum_{n=1}^{\infty} \frac{G_n}{n^3\pi^3} (-1)^n \quad (87)$$

$$\begin{aligned} D_w = & \frac{\partial}{\partial x} \left[8 \frac{\partial \bar{u}}{\partial x} \frac{\partial \zeta_e}{\partial x} (h + \zeta_e)^3 \sum_{n=1}^{\infty} \frac{G_n}{n^3\pi^3} (-1)^n \right. \\ & + 2 \frac{\partial \bar{u}}{\partial x} (h + \zeta_e)^4 \sum_{n=1}^{\infty} \frac{\partial G_n}{\partial x} \frac{(-1)^n}{n^2\pi^2} \\ & + \frac{13}{4} (h + \zeta_e)^3 \left(\frac{\partial \zeta_e}{\partial x} \right)^2 \sum_{n=1}^{\infty} \frac{G_n^2}{n^4\pi^4} \\ & + \frac{1}{2} (h + \zeta_e)^5 \sum_{n=1}^{\infty} \frac{1}{n^4\pi^4} \left(\frac{\partial G_n}{\partial x} \right)^2 \\ & + \frac{1}{6} (h + \zeta_e)^3 \left(\frac{\partial \zeta_e}{\partial x} \right)^2 \sum_{n=1}^{\infty} \sum_{\substack{m=1 \\ m \neq n}}^{\infty} \frac{G_n G_m}{nm\pi^4} \\ & \times \frac{2(n^2 + m^2) + 4(n^2 - m^2)\pi^2}{(n^2 - m^2)\pi^2} \\ & + \frac{5}{2} (h + \zeta_e)^4 \frac{\partial \zeta_e}{\partial x} \sum_{n=1}^{\infty} \frac{G_n}{n^4\pi^4} \frac{\partial G_n}{\partial x} + 2(h + \zeta_e)^4 \\ & \left. \times \frac{\partial \zeta_e}{\partial x} \sum_{n=1}^{\infty} \sum_{\substack{m=1 \\ m \neq n}}^{\infty} \frac{\partial G_n}{\partial x} \frac{G_m}{nm\pi^4} \frac{(-1)^{n+m}}{n^2 - m^2} \right] \quad (88) \end{aligned}$$

$$\begin{aligned} D_{uw} = & \frac{\partial^2}{\partial x^2} \left[(h + \zeta_e)^4 + \frac{\partial \bar{u}}{\partial x} \sum_{n=1}^{\infty} \frac{G_n}{n^3\pi^3} (-1)^n \right. \\ & + 2(h + \zeta_e)^3 \bar{u} \frac{\partial \zeta_e}{\partial x} \sum_{n=1}^{\infty} \frac{G_n}{n^3\pi^3} (-1)^n \\ & + (h + \zeta_e)^4 \bar{u} \sum_{n=1}^{\infty} \frac{\partial G_n}{\partial x} \frac{(-1)^n}{n^3\pi^3} \\ & + (h + \zeta_e)^3 \bar{u} \frac{\partial \zeta_e}{\partial x} \sum_{n=1}^{\infty} (1 + (-1)^n) \\ & + \frac{1}{2} (h + \zeta_e)^4 \frac{\partial \zeta_e}{\partial x} \sum_{n=1}^{\infty} \frac{G_n^2}{n^4\pi^4} \\ & - 2(h + \zeta_e)^4 \frac{\partial \zeta_e}{\partial x} \sum_{n=1}^{\infty} \sum_{\substack{m=1 \\ m \neq n}}^{\infty} \frac{G_n G_m}{nm\pi^4(n^2 - m^2)} \\ & + \frac{1}{4} (h + \zeta_e)^5 \sum_{n=1}^{\infty} \frac{G_n}{n^4\pi^4} \frac{\partial G_n}{\partial x} \\ & \left. - (h + \zeta_e)^5 \sum_{n=1}^{\infty} \sum_{\substack{m=1 \\ m \neq n}}^{\infty} \frac{G_n}{nm\pi^4} \frac{\partial G_m}{\partial x} \frac{1}{n^2 - m^2} \right] \end{aligned}$$

$$\begin{aligned} & - (h + \zeta_e)^4 \frac{\partial \zeta_e}{\partial x} \sum_{n=1}^{\infty} \frac{G_n^2}{n^2\pi^2} \left(\frac{1}{12} - \frac{1}{4n^2\pi^2} \right) \\ & + (h + \zeta_e)^4 \frac{\partial \zeta_e}{\partial x} \sum_{n=1}^{\infty} \sum_{\substack{m=1 \\ m \neq n}}^{\infty} \frac{G_n G_m}{nm\pi^4} \frac{(-1)^{n+m}}{(n + m)^2} \quad (89) \end{aligned}$$

References

- Cox, D.T., Kobayashi, N., 1997. Kinematic undertow model with logarithmic boundary layer. *J. Waterw., Port, Coast., Ocean Eng.* 123 (6), 354–360.
- Cox, D.T., Kobayashi, N., Okaiasu, A., 1995. Experimental and numerical modeling of surf zone hydrodynamics. Research Report CACR-95-07, Center For Applied Coastal Research. University of Delaware, USA.
- De Vriend, H.J., Stive, M.F.J., 1987. Quasi 3D modeling of nearshore currents. *Coast. Eng.* 11, 565–601.
- Gobbi, M.F., Kirby, J.T., 1999. Wave evolution over submerged sills: tests of a high order Boussinesq model. *Coast. Eng.* 37, 57–96.
- Hansen, J.B., Svendsen, I.A., 1979. Regular waves in shoaling water experimental data. Institute of Hydrodynamics and Hydraulic Engineering, Technical University of Denmark, p. 21.
- Jeong, J.H., Yang, D.Y., 1998. Finite element analysis of transient fluid flow with free surface using VOF (Volume-Of-Fluid) method and adaptive grid. *Int. J. Numer. Methods Fluids* 26, 1127–1154.
- Jeong, J.H., Yang, D.Y., 1999. Three dimensional finite element analysis of transient fluid flow with free-surface using marker surface method and adaptive grid refinement. *Int. J. Numer. Methods Fluids* 29, 657–684.
- Jha, A.K., Akiyama, J., Ura, M., 2001. High resolution flux-difference-splitting scheme on adaptive grid for open-channel flows. *Int. J. Numer. Methods Fluids* 36, 35–52.
- Kania, L., 1999. Elliptic adaptive grid generation and area equidistribution. *Int. J. Numer. Methods Fluids* 30, 481–491.
- Karambas, T.V., Koutitas, C., 1992. A breaking wave propagation model based on the Boussinesq equations. *Coast. Eng.* 18, 1–19.
- Karambas, T.V., Tozer, N.P., 2003. Breaking waves in the surf and swash zone. *J. Coast. Res.* 19, 514–528.
- Kennedy, A.B., Chen, Q., Kirby, J.T., Dalrymple, R.A., 2000. Boussinesq modeling of wave transformation, breaking and run-up: I. *1D. J. Waterw., Port, Coast., Ocean Eng.* 126, 39–47.
- Kennedy, A.B., Kirby, J.T., Chen, Q., Dalrymple, R.A., 2001. Boussinesq-type equations with improved nonlinear performance. *Wave Motion* 33, 225–243.
- Lie, K.-A., Haugse, V., Hvistendahl Karlsen, K., 1998. Dimensional splitting with front tracking and adaptive grid refinement. *Numer. Methods Partial Differ. Equ.* 14 (5), 627–648.
- Lin, J.C., 1994. Instantaneous structure of a breaking wave. *Phys. Fluids* 6 (9), 2877–2879.
- Lin, J.C., Rockwell, D., 1995. Evolution of a quasi-steady breaking wave. *J. Fluid Mech.* 302, 29–44.

- Madsen, P.A., Schäffer, H.A., 1998. Higher-order Boussinesq-type equations for surface gravity waves: derivation and analysis. *Philos. Trans. R. Soc. Lond., A* 356, 3123–3184.
- Madsen, P.A., Murray, R., Sørensen, O.R., 1991. A new form of the Boussinesq equations with improved linear dispersion characteristics. *Coast. Eng.* 15, 371–388.
- Madsen, P.A., Bingham, H.B., Liu, H., 2002. A new Boussinesq method for fully nonlinear waves from shallow to deep water. *J. Fluid Mech.* 462, 1–30.
- Melville, W.K., Veron, F., White, C.J., 2002. The velocity field under breaking waves: coherent structures and turbulence. *J. Fluid Mech.* 454, 203–233.
- Nadaoka, K., Hino, M., Koyano, Y., 1989. Structure of the turbulent flow field under breaking waves in the surf zone. *J. Fluid Mech.* 204, 359–387.
- Nwogu, O., 1993. Alternative form of Boussinesq equations for nearshore wave propagation. *J. Waterw., Port, Coast., Ocean Eng.* 6, 618–638.
- Papadakis, G., Bergeles, G., 1999. A local grid refinement method for three-dimensional turbulent recirculating flows. *Int. J. Numer. Methods Fluids* 31, 1157–1172.
- Park, K.-Y., Borthwick, A.G.L., 2001. Quadtree grid numerical model of nearshore wave-current interaction. *Coast. Eng.* 42, 219–239.
- Peregrine, D.H., 1966. Calculations of the development of an ondular bore. *J. Fluid Mech.* 25, 321–331.
- Schäffer, H.A., Madsen, P.A., Deigaard, R., 1993. A Boussinesq model for waves breaking in shallow water. *Coast. Eng.* 20, 185–202.
- Spitaleri, R.M., Corinaldesi, L., 1997. A multigrid semi-implicit finite difference method for the two dimensional shallow water equations. *Int. J. Numer. Methods Fluids* 25, 1229–1240.
- Svendsen, I.A., Veeramony, J., 2001. Wave breaking in wave groups. *J. Waterw., Port, Coast., Ocean Eng.* 127 (4), 200–212.
- Svendsen, I.A., Veeramony, J., Bakunin, J., Kirby, J.T., 2000. The flow in weak turbulent hydraulic jump. *J. Fluid Mech.* 418, 25–57.
- Ting, F.C.K., Kirby, J.T., 1996. Dynamics of surf-zone turbulence in a spilling breaker. *Coast. Eng.* 27, 131–160.
- Van Dongeren, A.R., Svendsen, I.A., 1997. Absorbing-generating boundary condition for shallow water models. *J. Waterw., Port, Coast., Ocean Eng.* 123 (6), 303–313.
- Veeramony, J., Svendsen, I.A., 2000. The flow in the surf-zone waves. *Coast. Eng.* 39, 93–122.
- Wei, G., Kirby, J.T., 1995. Time-dependent numerical code for extended Boussinesq equations. *J. Waterw., Port, Coast., Ocean Eng.* 121 (5), 251–261.
- Wei, G., Kirby, J.T., Grilli, S.T., Subramanya, R., 1995. A fully non linear Boussinesq model for surface waves. I. Highly non linear, unsteady waves. *J. Fluid Mech.* 294, 71–92.
- Witting, J.M., 1984. A unified model for the evolution of nonlinear water waves. *J. Comput. Phys.* 56, 203–236.
- Wu, J., Ritzdorf, H., Oosterlee, K., Steckel, B., Scüller, A., 1997. Adaptive parallel multigrid solution of 2D incompressible Navier–Stokes equations. *Int. J. Numer. Methods Fluids* 24, 875–892.
- Zelt, J.A., 1991. The run-up of nonbreaking and breaking solitary waves. *Coast. Eng.* 15, 205–246.